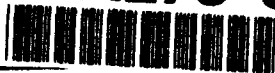


AD-A278 397



REPORT DATE

25 February 94

3. REPORT TYPE AND DATES COVERED

SBIR phase I, 1 Jul 93 - 31 Jan 94

## 4. TITLE AND SUBTITLE

Structural Integrity of Intelligent Materials and Structures

## 6. AUTHOR(S)

Warren C. Gibson  
Bryce L. Fowler

## 7. PERFORMING ORGANIZATION NAME(S) AND ADDRESS(ES)

CSA Engineering, Inc.  
2850 West Bayshore Road  
Palo Alto, CA 94303-3843

## 5. FUNDING NUMBERS

F49620-93-C-  
0026  
2302/DS8. PERFORMING ORGANIZATION  
REPORT NUMBER

AFOSR-TR- 04 0166

Report #94-02-05

## 9. SPONSORING/MONITORING AGENCY NAME(S) AND ADDRESS(ES)

U.S. Air Force Office of Scientific Research  
110 Duncan Ave., Suite B115  
Bolling AFB, DC 20332-000110. SPONSORING/MONITORING  
AGENCY REPORT NUMBERF49620-93-C-  
0026

## 11. SUPPLEMENTARY NOTES

SBIR Phase I Final Report

DTIC  
SELECTE  
APR 2 1994  
S B D

## 12a. DISTRIBUTION AVAILABILITY STATEMENT

Approved for public release,  
distribution unlimited

## 12b. DISTRIBUTION CODE

## 13. ABSTRACT (Maximum 200 words)

Intelligent materials open new avenues to improve performance, reliability, and longevity of future aerospace vehicle structures by allowing the materials themselves to become active elements for multiple system functions. However, the application of intelligent materials and structures has been inhibited because the effects of microstructural interactions between intelligent and host material elements have heretofore not been well characterized. This research implemented and applied three analytical approaches to the study of stress concentrations and cracking around embedded sensor/actuator elements. One was an analytical method based on high-order Ritz functions for accurate representation of steep strain gradients. The second was a conventional finite element approach using very fine meshes, and the third was a finite-element-based computation of energy release rates suitable for predicting crack growth. Among other interesting results, the analyses compared the effects of applied loads with the effects of actuation strains and found that the applied loads were more likely to cause cracking or delamination than actuation.

## 14. SUBJECT TERMS

RITZ FUNCTIONS, Aerospace  
VEHICLE STRUCTURES

## 15. NUMBER OF PAGES

42

## 16. PRICE CODE

17. SECURITY CLASSIFICATION  
OF REPORT

Unclassified

18. SECURITY CLASSIFICATION  
OF THIS PAGE

Unclassified

19. SECURITY CLASSIFICATION  
OF ABSTRACT

Unclassified

## 20. LIMITATION OF ABSTRACT



Engineering Services in Structural Dynamics

2850 W. Bayshore Road Palo Alto, California 94303-3843

(415) 494-7351 Fax: (415) 494-8749

**Structural Integrity of Intelligent  
Materials and Structures**

**Submitted To:**

**U. S. Air Force Office of Scientific Research  
Washington, DC**

**Contract F49620-93-C-0026**

**Report No. 94-02-05**

**February 1994**

This report documents a Phase I SBIR research effort conducted by CSA Engineering, Inc. and its subcontractor, Mr. Marc Regelbrugge, under Air Force contract F49620-93-C-0026. The research was conducted during the period 1 Jul 93 to 31 Jan 94. CSA gratefully acknowledges Mr. Regelbrugge's contributions which were essential to all aspects of the program

Prepared by: Warren C. Gibson  
Warren C. Gibson, Ph.D.  
Principal Engineer

Bryce L. Fowler  
Bryce L. Fowler  
Engineer

Accession For	
NTIS GRA&I	<input checked="checked" type="checkbox"/>
DTIC TAB	<input type="checkbox"/>
Unannounced	<input type="checkbox"/>
Justification	
By	
Distribution/	
Availability Codes	
Dist	Avail and/or Special
A-1	

## Contents

<b>1. Introduction</b>	<b>1</b>
1.1 Objective and Scope of Effort . . . . .	1
1.2 Summary of Work Performed . . . . .	1
<b>2. Task 1 – Interface Models</b>	<b>3</b>
2.1 Analytical Model Formulation . . . . .	4
2.2 Analytical Model Implementation . . . . .	10
<b>3. Task 2 – Models of Embedded Elements</b>	<b>11</b>
3.1 Analytical Models . . . . .	11
3.1.1 Description . . . . .	11
3.1.2 Interface Strain Field Predictions . . . . .	12
3.1.3 Influence of Host-Material Orientation . . . . .	17
3.1.4 Requirements for Model Discretization . . . . .	18
3.2 Finite Element Models . . . . .	20
3.2.1 Intralayer Embedment . . . . .	20
3.2.2 Interlayer Embedment . . . . .	24
<b>4. Task 3 – Interface Failure Models</b>	<b>28</b>
4.1 Calculation of Strain-Energy Release Rates . . . . .	28
4.2 Virtual Crack Extension . . . . .	29
4.2.1 Theory . . . . .	29
4.2.2 Development . . . . .	31
4.2.3 Programming . . . . .	32
4.3 Results . . . . .	33
4.3.1 Intralayer Embedded Element . . . . .	33
4.3.2 Interlayer Embedded Element . . . . .	34
<b>5. Task 4 – Candidate Experimental Configurations</b>	<b>38</b>
5.1 Requirements . . . . .	38
5.2 Sensing Approaches . . . . .	38
5.3 Discussion . . . . .	39
<b>6. Conclusions</b>	<b>40</b>

6.1	Observations . . . . .	40
6.2	Evaluation of Approach and Results . . . . .	41

## List of Figures

1	I-J Analytical-Model Topology (* - $i, j$ indices in parentheses) . . . .	4
2	Analytical Interface-Stress Model Configuration . . . . .	12
3	Axial Strains along Interlaminar Interface . . . . .	14
4	Through-Thickness Strains along Interlaminar Interface . . . . .	14
5	Shear Strains along Interlaminar Interface . . . . .	15
6	Interface Axial Strains through Laminate Thickness . . . . .	15
7	Interface Through-Thickness Strains through Laminate Thickness . .	16
8	Interface Shear Strains through Laminate Thickness . . . . .	16
9	Strain Concentration vs. Lamination Angle – Applied Stress Loading	17
10	Strain Concentration vs. Lamination Angle – Induced Strain Loading	18
11	Strain Concentration vs. Stiffness Ratio – Applied Stress Loading . .	19
12	Strain Concentration vs. Stiffness Ratio – Induced Strain Loading . .	19
13	Intralayer embedded FEM model . . . . .	20
14	Shear strains in the initial FEM model . . . . .	22
15	Nodal displacements with no horizontal nodes released . . . . .	22
16	Nodal displacements with one horizontal nodes released . . . . .	23
17	Nodal displacements with four horizontal nodes released . . . . .	23
18	Interlayer embedded FEM model . . . . .	24
19	Nodal displacements with no nodes released; axial load in tension . .	26
20	Nodal displacements with no nodes released; axial load in compression	26
21	Nodal displacements with four nodes released; axial load in compression	27
22	Quantities for Calculating Strain Energy Release Rates . . . . .	28
23	Virtual Crack Extension Computation of Strain Energy Release Rate	30
24	Intralayer Embedded Strain Energy Release Rates . . . . .	33
25	Intralayer-Embedded Mode II Strain Energy Release Rate Ratio . . .	35
26	Interlayer-Embedded Assumed Crack Locations . . . . .	35
27	Strain Energy Release Rates along Piezoelectric Wafer Interface . . .	36
28	Strain Energy Release Rates along Composite Interface . . . . .	37

## List of Tables

1	Analytical Model Material Properties . . . . .	11
2	Interfacial Strain Concentrations . . . . .	13

## **1. Introduction**

### **1.1 Objective and Scope of Effort**

This work was performed in response to topic AF93-015, "Structural Integrity of Intelligent Materials and Structures." Intelligent materials open new avenues to improve performance reliability, and longevity of future aerospace vehicle structures by allowing the structural materials themselves to become active elements for multiple system functions. However, the application of these materials and structures has been inhibited because the effects of microstructural interactions between intelligent and host material elements have not yet been well characterized. The research described here was to develop predictive models of these local phenomena to enable analytical assessment of their effects on material and structural integrity. The work focused on interfacial loadings and propagation of interface failures in intelligent material systems with embedded active elements. Detailed analytical and finite-element models were developed and employed to assess these effects. As a result, some key characteristics governing failure mechanisms in these systems have come to light.

The case studies encompassed a class of likely application scenarios involving embedment of piezoelectric ceramic wafers in conventional polymer-matrix composites. Two particular configurations were examined. The first had a piezoceramic replacing part of one composite layer ("intralayer embedment") while the second had the active wafer inserted between layers, thus causing a bulge in the material ("interlayer embedment"). Stress and strain concentrations were examined in detail for regions near interfaces between the embedded and host materials. Finite-element models were used to assess interfacial crack growth behavior both between the piezoelectric element and the host material, and between layers of the host material.

The results of these studies indicate that while mode I (interlaminar tension) responses to activation of the piezoelectric wafer may contribute to the initiation of interface cracks, crack propagation is, at least for the cases examined, governed by mode II (interlaminar shear) behavior within the host composite and at the interface between intelligent and host materials.

### **1.2 Summary of Work Performed**

The work done under this project has:

1. Developed a general, two-dimensional analytical method to assess stress and strain gradients at interfaces within intelligent material systems. The method was implemented in a computer program was written and applied successfully.
2. Developed detailed finite-element models of composite materials incorporating embedded intelligent material elements.

3. Implemented the virtual crack extension method, based on NASTRAN finite element models, for assessing crack growth by direct computation of energy release rates.
4. Examined the relative severity of stress and strain concentrations subject to the influence of externally applied loads as well as induced-strain activation of the intelligent material element
5. Assessed the influence of composite lamination angle on the severity of local stress gradients.
6. Assessed factors contributing to the onset and propagation of interfacial cracks in intelligent material systems.
7. Considered some requirements and approaches for experimental characterization of interfacial crack propagation in intelligent material systems.

Sections 2 through 5 discuss the four tasks that were defined in the proposal, the work that was done, and the results that were obtained for some representative configurations. Section 6 presents conclusions.



## 2. Task 1 – Interface Models

Analytical models were developed to allow rapid assessment of the severity of local strain gradients caused by embedment of intelligent material elements in composite host materials, and to guide development of finite-element models used subsequently to assess fracture behavior of these systems. The analytical models were based on variable-order power-series expansions of structural displacements in two dimensions. High-order models were employed to predict strain gradients at interfaces between dissimilar materials in the intelligent material systems.

A variational formulation was used to derive the governing equations for the analytical model. The resulting equations for the unknown coefficients were straightforwardly organized into a linear algebraic system and solved numerically. Displacements, strains and stresses were then computed from the power-series expansions and their derivatives.

The variational condition is

$$\delta(U - W) = 0 \quad (1)$$

where  $U$  and  $W$  are strain energy and work terms, respectively. The strain energy is expressed in terms of appropriate derivatives of the assumed displacement fields. The work term involves integrals of the applied surface tractions and corresponding surface displacements.

$$\begin{aligned} U &= \frac{1}{2} \int_V (\epsilon - \epsilon^p)^T C (\epsilon - \epsilon^p) dV \\ W &= \int_S f^T d dS \end{aligned} \quad (2)$$

Differentiating the above integrals with respect to the unknown series coefficients results in a governing equation for each coefficient. These governing equations are assembled into an algebraic system of equations and solved numerically.

The problem addressed under this project considered a number of rectilinear regions adjoined at their boundaries. The approach was to divide the composite material system into such regions near the interfaces of interest. Each region comprised a single material, and each region retained its own local displacement expansion. The regions form a rectilinear grid, or mesh, wherein each individual region was identified by two coordinate indices (I-J). The I-J topology, shown in Figure 1, admitted modeling of both embedded and surface-attached active-material elements.

Since the series expansions employed are continuous beyond first derivatives, they are useful only within a single-material region. Thus, matching conditions were developed to link solutions along region boundaries representing interfaces between dissimilar materials. These matching conditions were implemented using Lagrange mul-

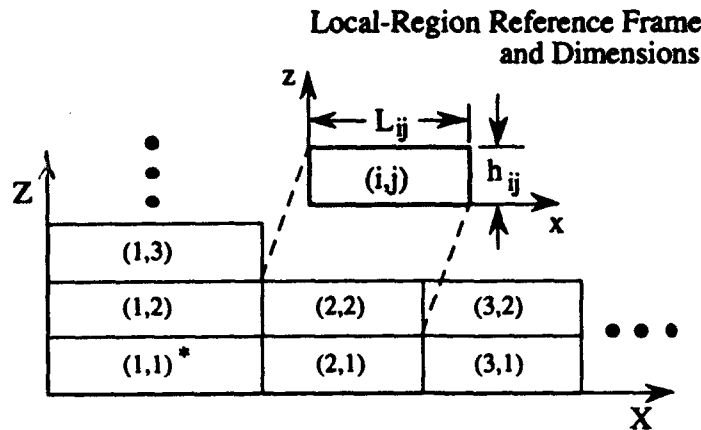


Figure 1: I-J Analytical-Model Topology (\* -  $i, j$  indices in parentheses)

multipliers to preserve simplicity and numerical precision in their implementation. The Lagrange multiplier method also yields exact satisfaction of the matching conditions.

The two-dimensional model considered surface tractions in the normal and tangential directions, allowing specification of all admissible boundary-stress components. Displacement boundary conditions were limited to geometric symmetry conditions on chosen model boundaries.

The following sections describe details of the analytical model formulation and implementation.

## 2.1 Analytical Model Formulation

The analytical interface model developed under this project was based on a power-series expansion of displacement fields in two dimensions. Displacements ( $u, w$ ) in the  $xz$ -plane were assumed to be of the form

$$\begin{aligned} u(x, z) &= a_{00} + a_{m0}(x/\ell)^m + a_{0n}(z/h)^n + a_{mn}(x/\ell)^m(z/h)^n \\ w(x, z) &= b_{00} + b_{m0}(x/\ell)^m + b_{0n}(z/h)^n + b_{mn}(x/\ell)^m(z/h)^n \end{aligned} \quad (3)$$

The quantities  $\ell$  and  $h$  are characteristic spatial lengths in the  $x$ - and  $z$ -directions, respectively, and the coefficients  $a$  and  $b$  are to be determined. Equations (2) assume the summation convention over repeated indices:  $m = 1 \dots M$ ,  $n = 1 \dots N$ .

Using (3), strains linear and boundary displacements were derived for a chosen order of approximation ( $M, N$ ). The linear, *total* strain tensor was defined, using contracted notation, as

$$\epsilon = \begin{Bmatrix} \epsilon_1 + \epsilon_1^p \\ \epsilon_3 + \epsilon_3^p \\ \gamma_5 \end{Bmatrix}$$

where the  $\epsilon_i$  are mechanical strains, and the  $\epsilon_i^p$  are pre-strains induced by thermal and/or electrical fields (assumed constant within each region).

Setting

$$\lambda = \frac{1}{\ell}, \quad \zeta = \frac{1}{h}, \quad \text{and} \quad a_{mn}, b_{mn} \equiv 0 \quad (m > M \text{ or } n > N),$$

displacements and their spatial derivatives can be written

$$\begin{aligned} u &= a_{00} + a_{m0}(\lambda x)^m + a_{0n}(\zeta z)^n + a_{mn}(\lambda x)^m(\zeta z)^n \\ u_{,x} &= \lambda [a_{10} + a_{1n}(\zeta z)^n] + \lambda(m+1) [a_{(m+1)0}(\lambda x)^m + a_{(m+1)n}(\lambda x)^m(\zeta z)^n] \\ u_{,z} &= \zeta [a_{01} + a_{m1}(\lambda x)^m] + \zeta(n+1) [a_{0(n+1)}(\zeta z)^n + a_{m(n+1)}(\lambda x)^m(\zeta z)^n] \\ w &= b_{00} + b_{m0}(\lambda x)^m + b_{0n}(\zeta z)^n + b_{mn}(\lambda x)^m(\zeta z)^n \\ w_{,x} &= \lambda [b_{10} + b_{1n}(\zeta z)^n] + \lambda(m+1) [b_{(m+1)0}(\lambda x)^m + b_{(m+1)n}(\lambda x)^m(\zeta z)^n] \\ w_{,z} &= \zeta [b_{01} + b_{m1}(\lambda x)^m] + \zeta(n+1) [b_{0(n+1)}(\zeta z)^n + b_{m(n+1)}(\lambda x)^m(\zeta z)^n] \end{aligned}$$

Taking the liberty to define  $0^0 \equiv 1$  allows these quantities to be expressed more compactly as

$$\left. \begin{aligned} u &= a_{mn}(\lambda x)^m(\zeta z)^n \\ u_{,x} &= \lambda(m+1)a_{(m+1)n}(\lambda x)^m(\zeta z)^n \\ u_{,z} &= \zeta(n+1)a_{m(n+1)}(\lambda x)^m(\zeta z)^n \\ w &= b_{mn}(\lambda x)^m(\zeta z)^n \\ w_{,x} &= \lambda(m+1)b_{(m+1)n}(\lambda x)^m(\zeta z)^n \\ w_{,z} &= \zeta(n+1)b_{m(n+1)}(\lambda x)^m(\zeta z)^n \end{aligned} \right\} (m = 0 \dots M, n = 0 \dots N). \quad (4)$$

The mechanical strains are then

$$\begin{aligned} \epsilon_1 &= u_{,x} - \epsilon_1^p \\ \epsilon_3 &= w_{,z} - \epsilon_3^p \\ \gamma_5 &= u_{,z} + w_{,x} \end{aligned} \quad (5)$$

where contracted notation is used for the strain components and the quantities  $\epsilon_1^p$  and  $\epsilon_3^p$  are pre-strains representing a combination of thermal and/or electrically induced strains.

The analytical model assumed a transversely isotropic material with isotropy in the  $xz$  plane. Thus, the strain energy within a region was expressed as

$$U = \frac{1}{2} \int_0^h \int_0^\ell [C_{11}(u_{,x} - \epsilon_1^p)^2 + C_{33}(w_{,z} - \epsilon_3^p)^2 + 2C_{13}(u_{,x} - \epsilon_1^p)(w_{,z} - \epsilon_3^p) + C_{55}\gamma_5^2] dz dx \quad (6)$$

Applied tractions were also expressed as power-series expansions

$$\left. \begin{aligned} \bar{\sigma}_1(\ell, z) &= s_k(\zeta z)^k \\ \bar{\tau}_5(\ell, z) &= t_k(\zeta z)^k \\ \bar{\sigma}_3(x, h) &= r_j(\lambda x)^j \\ \bar{\tau}_5(x, h) &= q_j(\lambda x)^j \end{aligned} \right\} (j = 0 \dots M, k = 0 \dots N). \quad (7)$$

allowing the work integral to be expressed as

$$W = \int_0^h [\bar{\sigma}_1(\ell, z) \cdot u(\ell, z) + \bar{\tau}_5(\ell, z) \cdot w(\ell, z)] dz + \int_0^\ell [\bar{\sigma}_3(x, h) \cdot w(x, h) + \bar{\tau}_5(x, h) \cdot u(x, h)] dx \quad (8)$$

Inter-region displacement compatibility and symmetric boundary conditions were enforced by means of Lagrange multipliers. The compatibility conditions enforced were

$$\left. \begin{aligned} u(0, z)^{(i+1)j} &= u(\ell, z)^{ij} \\ u(x, 0)^{i(j+1)} &= u(x, h)^{ij} \\ w(0, z)^{(i+1)j} &= w(\ell, z)^{ij} \\ w(x, 0)^{i(j+1)} &= w(x, h)^{ij} \end{aligned} \right\} \quad (9)$$

The boundary conditions enforced were

$$\left. \begin{aligned} u(0, z)^{1j} &= 0 \\ w_{,x}(0, z)^{1j} &= 0 \\ u_{,z}(x, 0)^{i1} &= 0 \\ w(x, 0)^{i1} &= 0 \end{aligned} \right\} \quad (10)$$

The resulting Lagrangian functions used to augment the energy functional were, for the matching conditions,

$$\begin{aligned}
 g_{ux}^{(i+1)j} [u(0, z)^{(i+1)j} - u(\ell, z)^{ij}] &= 0 \\
 g_{ux}^{i(j+1)} [u(x, 0)^{i(j+1)} - u(x, h)^{ij}] &= 0 \\
 g_{wz}^{(i+1)j} [w(0, z)^{(i+1)j} - w(\ell, z)^{ij}] &= 0 \\
 g_{wz}^{i(j+1)} [w(x, 0)^{i(j+1)} - w(x, h)^{ij}] &= 0
 \end{aligned} \tag{11}$$

and, for the boundary conditions,

$$\begin{aligned}
 g_{uz}^{1j} u(0, z)^{1j} &= 0 \\
 g_{wz}^{1j} w, x(0, z)^{1j} &= 0 \\
 g_{ux}^{i1} u, z(x, 0)^{i1} &= 0 \\
 g_{wx}^{i1} w(x, 0)^{i1} &= 0
 \end{aligned} \tag{12}$$

where the  $g_{\xi\eta}$  are unknown Lagrange multipliers.

Expressions (6), (8), (11) and (12) were assembled into the energy functional (1) using the displacement and boundary-force expansions (3) and (7). The resulting integrals were evaluated analytically, and differentiated with respect to each of the unknown coefficients  $a_{mn}$ ,  $b_{mn}$  and  $g_{\xi\eta}$  to minimize the energy functional.

Analytical integrals of the energy functional constituents were easily derived from the polynomial forms of the assumed strain fields and applied boundary forces. Volume integrals involve terms of the form

$$\int_0^h \int_0^\ell (\lambda x)^{m+j} (\zeta z)^{n+k} dx dz$$

for products of coefficients  $a_{mn}$  or  $b_{mn}$  with coefficients  $a_{jk}$  or  $b_{jk}$ . These terms integrate to

$$\int_0^h \int_0^\ell (\lambda x)^{m+j} (\zeta z)^{n+k} dx dz = \frac{(\lambda x)^{m+j+1} (\zeta z)^{n+k+1}}{\lambda \zeta (m+j+1)(n+k+1)}$$

for the product of the  $mn^{th}$  and  $jk^{th}$  coefficients.

The work terms (surface integrals) involve integrals like

$$\int_0^h \left[ s_k \sum_m a_{mn} (\zeta z)^{n+k} \right] dz.$$

with the result

$$\int_0^h \left[ s_k \sum_m a_{mn} (\zeta z)^{n+k} \right] dz = \sum_m \frac{s_k a_{mn}}{\zeta (n+k+1)}.$$

Differentiating the above integrals with respect to the unknown coefficients results in the following nontrivial equations for each region.

$$\begin{aligned}
 \frac{\partial}{\partial a_{mn}} \left[ \frac{1}{2} \int_0^h \int_0^\ell C_{11} (u_{,x} - \epsilon_1^p)^2 dx dz \right] &= \\
 C_{11} \left[ \frac{\lambda m j}{\zeta(m+j-1)(n+k+1)} a_{jk} - \frac{\epsilon_1^p}{\zeta(n+1)} \right] \\
 \frac{\partial}{\partial b_{mn}} \left[ \frac{1}{2} \int_0^h \int_0^\ell C_{33} (w_{,z} - \epsilon_3^p)^2 dx dz \right] &= \\
 C_{33} \left[ \frac{\zeta n k}{\lambda(m+j+1)(n+k-1)} b_{jk} - \frac{\epsilon_3^p}{\lambda(m+1)} \right] \\
 \frac{\partial}{\partial a_{mn}} \left[ \frac{1}{2} \int_0^h \int_0^\ell 2C_{13} (u_{,x} - \epsilon_1^p)(w_{,z} - \epsilon_3^p) dx dz \right] &= \\
 C_{13} \left[ \frac{mk}{(m+j)(n+k)} b_{jk} - \frac{\epsilon_3^p}{\zeta(n+1)} \right] \\
 \frac{\partial}{\partial b_{mn}} \left[ \frac{1}{2} \int_0^h \int_0^\ell 2C_{13} (u_{,x} - \epsilon_1^p)(w_{,z} - \epsilon_3^p) dx dz \right] &= \\
 C_{13} \left[ \frac{jn}{(m+j)(n+k)} a_{jk} - \frac{\epsilon_1^p}{\lambda(m+1)} \right] \\
 \frac{\partial}{\partial a_{mn}} \left[ \frac{1}{2} \int_0^h \int_0^\ell C_{55} (u_{,z} + w_{,x}) dx dz \right] &= \\
 C_{55} \left[ \frac{\zeta n k}{\lambda(m+j+1)(n+k-1)} a_{jk} + \frac{jn}{(m+j)(n+k)} b_{jk} \right] \\
 \frac{\partial}{\partial b_{mn}} \left[ \frac{1}{2} \int_0^h \int_0^\ell C_{55} (u_{,z} + w_{,x}) dx dz \right] &= \\
 C_{55} \left[ \frac{mk}{(m+j)(n+k)} a_{jk} + \frac{\lambda m j}{\lambda(m+j-1)(n+k+1)} b_{jk} \right] \\
 \frac{\partial}{\partial a_{mn}} \int_0^h \left[ s_k \sum_m a_{mn} (\zeta z)^{(n+k)} \right] dz &= \frac{s_k}{\zeta(n+k+1)} \\
 \frac{\partial}{\partial a_{mn}} \int_0^h \left[ t_k \sum_m a_{mn} (\zeta z)^{(n+k)} \right] dz &= \frac{t_k}{\zeta(n+k+1)} \\
 \frac{\partial}{\partial b_{mn}} \int_0^\ell \left[ r_k \sum_m b_{mn} (\lambda x)^{(m+k)} \right] dx &= \frac{r_k}{\lambda(m+k+1)}
 \end{aligned} \tag{13}$$

$$\frac{\partial}{\partial b_{mn}} \int_0^{\ell} \left[ q_k \sum_m b_{mn} (\lambda x)^{(m+k)} \right] dx = \frac{q_k}{\lambda(m+k+1)}$$

The compatibility constraint relations (11) take the following form:

$$\begin{aligned} g_{un}^{(i+1)j} (a_{0n}^{(i+1)j} - \sum_m a_{mn}^{ij}) &= 0 \\ g_{um}^{i(j+1)} (a_{m0}^{i(j+1)} - \sum_n a_{mn}^{ij}) &= 0 \\ g_{wn}^{(i+1)j} (b_{0n}^{(i+1)j} - \sum_m b_{mn}^{ij}) &= 0 \\ g_{wm}^{i(j+1)} (b_{m0}^{i(j+1)} - \sum_n b_{mn}^{ij}) &= 0 \end{aligned} \quad (14)$$

The boundary constraint relations (12) take the form:

$$\begin{aligned} g_{un}^{1j} a_{0n}^{1j} &= 0 \\ g_{um}^{i1} a_{m1}^{i1} &= 0 \\ g_{wn}^{i1} b_{m0}^{i1} &= 0 \\ g_{wn}^{1j} b_{1n}^{1j} &= 0 \end{aligned} \quad (15)$$

These expressions are straightforwardly differentiated with respect to  $a_{mn}$ ,  $b_{mn}$  and  $g_{\xi\eta}$  coefficients.

The above differentiated expressions comprise a set of  $2(M+1)(N+1)$  equations for the displacement-expansion coefficients  $a_{mn}$  and  $b_{mn}$  in each region. In addition, each region is associated with  $2(M+N+2)$  Lagrange multipliers to enforce boundary and matching conditions. These equations are assembled into a symmetric, linear algebraic system of equations for the entire structure to be modeled, and the system of equations is solved subject to prescribed boundary forces and/or imposed internal strains ( $\epsilon_i^p$ ).

The order of the displacement-expansion approximation is set by choosing values  $M$  and  $N$  for each region, with the restrictions that  $M_{ij}$  be the same for all regions with the same  $i$ -index, and that  $N_{ij}$  be the same for all regions with the same  $j$ -index. In practice,  $M$  and  $N$  values were set the same for all modeled regions, although  $M$  was not, in general, set to equal  $N$ .

One should note that the parameters  $M$  and  $N$  control the fidelity of the solution provided by the analytical model. In general, these solutions will be subject to truncation errors unless very high-order approximations are used. In the present effort, convergence behavior of the analytical model was studied, and resulted in the selection of  $M = 9$ ,  $N = 4$  for the material configurations considered (see §3.1).

## 2.2 Analytical Model Implementation

The analytical model described in the previous section was implemented in a C-language computer program. The program is written in standard, ANSI-C, and may be run on any computer having an ANSI-C compiler. For this project, the analytical model was implemented on an Apple Macintosh IIci computer.

Two principal advantages were found in using the analytical model. First, since the model addresses only a specific problem, it executes much faster than models of equivalent fidelity implemented in commercial finite-element programs. This makes the analytical model practical for assessing the effects of configuration variables such as material-layer thicknesses and layup angles. Second, the model converges rapidly on smooth descriptions of the high strain gradients occurring at material interfaces. This allows the model to be used, as it was in the present study, to guide the discretization of more general, finite-element models for detailed stress and fracture predictions (see §3.1.4).

The analytical model implemented here could be improved for faster, more general operation. For example, the Lagrange multiplier implementation of boundary conditions could be simplified by eliminating prescribed boundary unknowns directly before assembly of the governing equations. Also, more general boundary and interface conditions (e.g., internal free surfaces) could be implemented to allow modeling of fracture and delamination behavior. Finally, the power-series representation of displacement fields allows analytical integration of nonlinear strains to be implemented with relative ease. This would allow the model to treat geometrically nonlinear behavior as well.



Table 1: Analytical Model Material Properties

Property	Value	
	SI Units	English Units
Composite Moduli		
$E_{11}$	127 GPa	18.4 Msi
$E_{33}$	10 GPa	1.5 Msi
$G_{31}$	5.8 GPa	0.85 Msi
$\nu_{13}$	0.29	0.29
Piezoelectric Moduli		
$E_{11}$	88 GPa	12.8 Msi
$E_{33}$	66 GPa	9.6 Msi
$G_{31}$	29 GPa	4.2 Msi
$\nu_{13}$	0.31	0.31
Induced Strain:		
$d_{13}$	-122 pC/N	
$d_{33}$	285 pC/N	

### 3. Task 2 – Models of Embedded Elements

The analytical model described in the previous section was employed along with detailed finite-element models to assess structural responses and fracture behavior near interfaces between intelligent and host composite material elements. The models employed in this investigation, and results obtained from them, are described in this section. The results presented consist of predictions of interfacial strain concentrations for various host-material orientations, assessment of discretization requirements for finite-element models of the interface regions, and finite-element predictions of local strain gradients near material interfaces.

#### 3.1 Analytical Models

##### 3.1.1 Description

The analytical model was applied to the configuration shown in Figure 2 to assess local strain distributions. This model represents a piezoelectric wafer embedded within a layer of a thin, high-strength, graphite-epoxy laminate. The properties employed for each material are listed in Table 1.

The model was loaded by a combination of piezoelectric induced strains and an

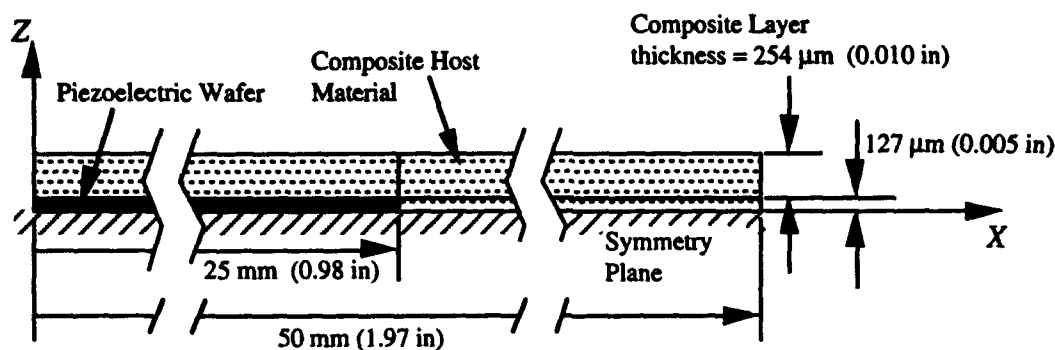


Figure 2: Analytical Interface-Stress Model Configuration

axial stress of 100 MPa (14.5 ksi). The piezoelectric strains corresponded to an applied electric field of 400 kV/m across the 0.254 mm-thick wafer, resulting in applied strains  $\epsilon_1^p = -48 \cdot 10^{-6}$  and  $\epsilon_3^p = 112 \cdot 10^{-6}$ .

The analytical models were exercised for two purposes. First, the analytical models were used to determine the effect of lamination angle on the severity of resulting strain gradients. This analysis was undertaken to study design modifications that might result in less-severe strain concentrations at material interfaces. Second, strain gradients were predicted to determine suitable discretizations for subsequent finite-element analyses. This was undertaken to ensure that finite-element models employed to assess crack-growth behavior in the intelligent material system would provide accurate results.

### 3.1.2 Interface Strain Field Predictions

The configuration shown in Figure 2 was analyzed for two cases: an applied axial stress loading of 100 MPa, and applied piezoelectric strains  $\epsilon_1^p = -48 \cdot 10^{-6}$  and  $\epsilon_3^p = 112 \cdot 10^{-6}$ . The results of these analyses are shown in Figures 3 to 8. Figures 3 to 5 show strain distributions along the length of the interlaminar interface at the top of the piezoelectric wafer ( $z = 0.127$  mm) as a function of distance from the symmetry plane imposed at  $x = 0$ . Figures 6 to 8 show strain distributions through the thickness of the model at the interface between the embedded piezoelectric wafer and the host material ( $x = 0.025$  m) and from the midplane ( $z = 0$ ) to the upper (free) surface. In these figures, the legend "Force Loading" refers to application of the 100 MPa axial stress, and the legend "Strain Loading" refers to the case where piezoelectric strains are prescribed. The "upper face" designation refers to strains in the composite host material just above the interface ( $z = 0.127+$  mm), while the "lower face" designation refers to strain distributions just below the interlaminar interface ( $z = 0.127-$  mm). The "+X" and "-X" designations refer to locations either

Table 2: Interfacial Strain Concentrations

Strain Measure (%)	100 MPa Loading	$\epsilon^p$ Loading
$ \epsilon_1^{\text{peak}} - \epsilon_1^{\text{avg}} $	0.012	0.001
$ \epsilon_3^{\text{peak}} - \epsilon_3^{\text{avg}} $	0.029	0.010
$ \gamma_5^{\text{peak}} $	0.066	0.0092

side of the interface at ( $x = 0.025$  m), with the “-X” referring to the side containing the piezoelectric wafer.

Examination of Figures 3 to 8 reveals some important aspects of the material system's elastic behavior. First and foremost, strain concentrations at the interfaces are influenced far more by the application of the 100 MPa mechanical stress than by the applied piezoelectric strains. Naturally, the magnitudes of these concentrations will depend directly on the magnitude of the applied loading. However, the 100 MPa applied stress represents roughly 10% of the composite material's ultimate strength, while the piezoelectric applied strains represent roughly 50% of that material's actuation capability. Table 2 lists peak strain concentrations for the two loading cases. Examination of this table shows that the integrity of the intelligent material system will be most affected by the external loading environment. Only in cases where external loads are small will induced-strain effects cause the worst interfacial stresses.

Table 2 shows that shear strain concentrations are the most severe under applied in-plane loadings, but through-thickness strain concentrations are slightly more severe when only induced-strain loading is present. From these results, one might expect the action of the intelligent material to have an appreciable effect on mode I (tension) interlaminar crack initiation, but subsequent crack growth would be heavily influenced by mode II (shear) behavior.

Another observation to be drawn from the model predictions is that the characteristic lengths of the strain concentrations are very small, typically of the order of 1-1.5 mm. (4-6 layer thicknesses). Also, both through-thickness ( $\epsilon_3$ ) and shear ( $\gamma_5$ ) strain gradients exhibit reversals with increased distance from the interface. The magnitude of the through-thickness strain reversal is roughly 0.002% (one-tenth of the strain concentration magnitude), and the magnitude of the shear strain reversal is roughly 0.005% (less than one-tenth of the strain concentration magnitude).

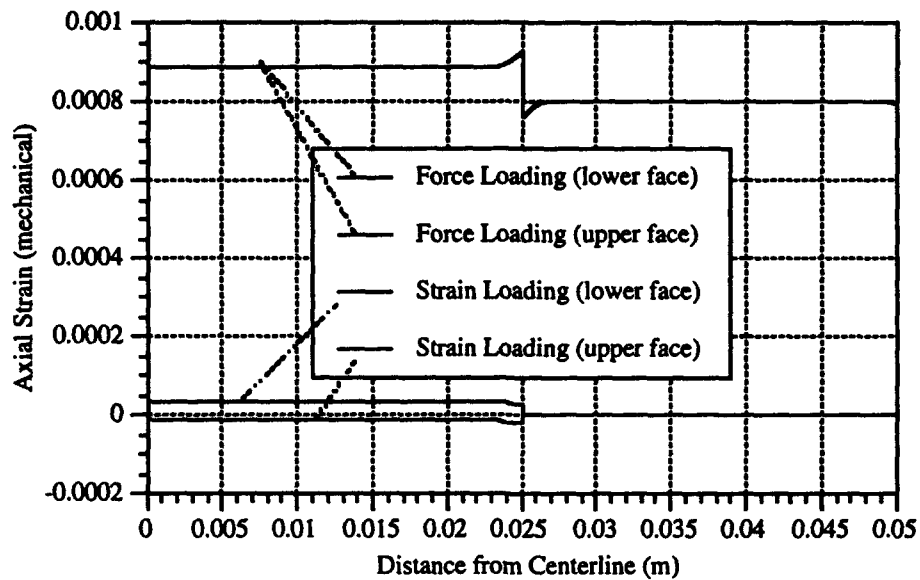


Figure 3: Axial Strains along Interlaminar Interface

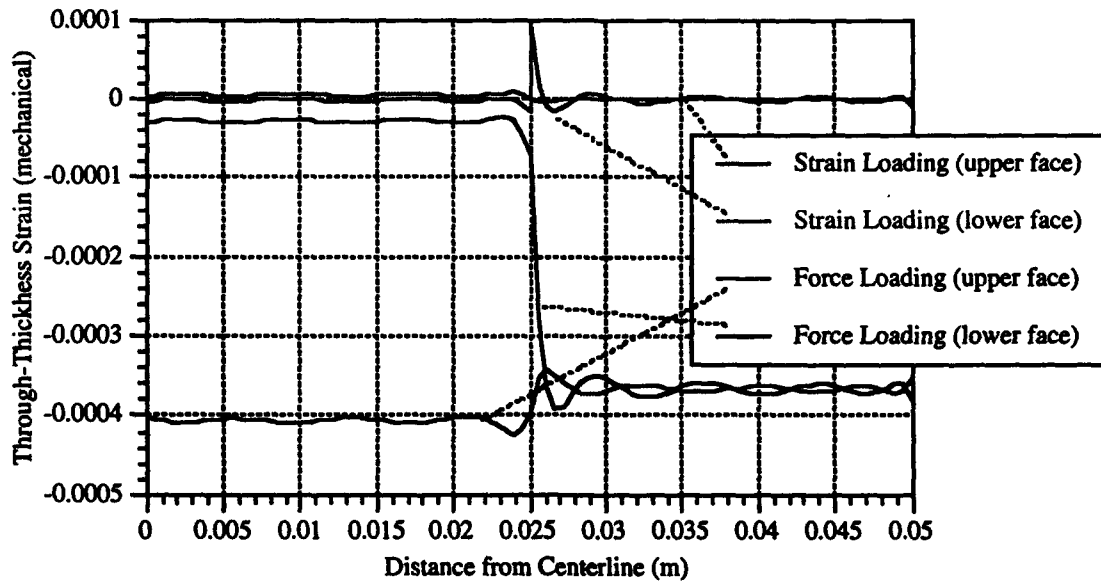


Figure 4: Through-Thickness Strains along Interlaminar Interface

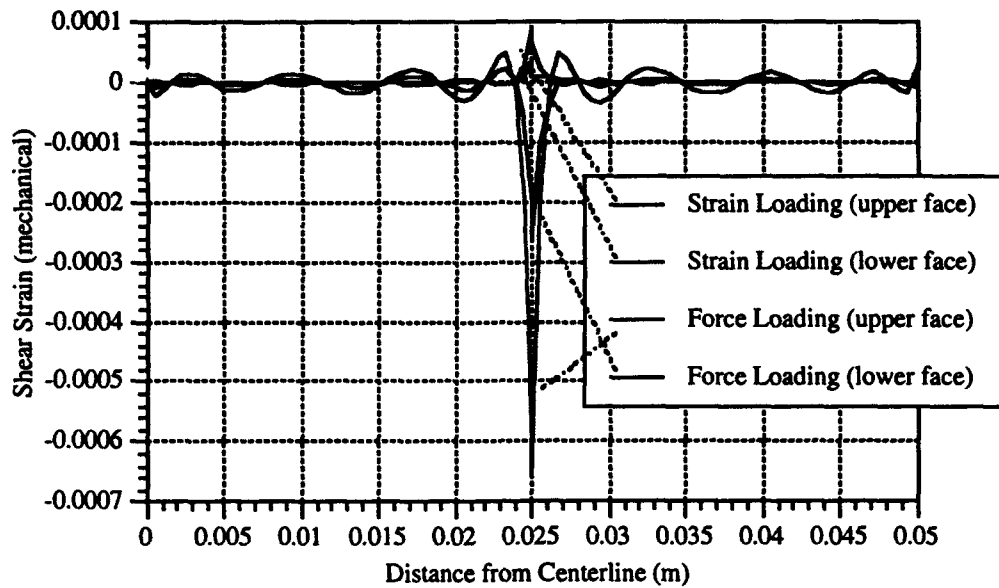


Figure 5: Shear Strains along Interlaminar Interface

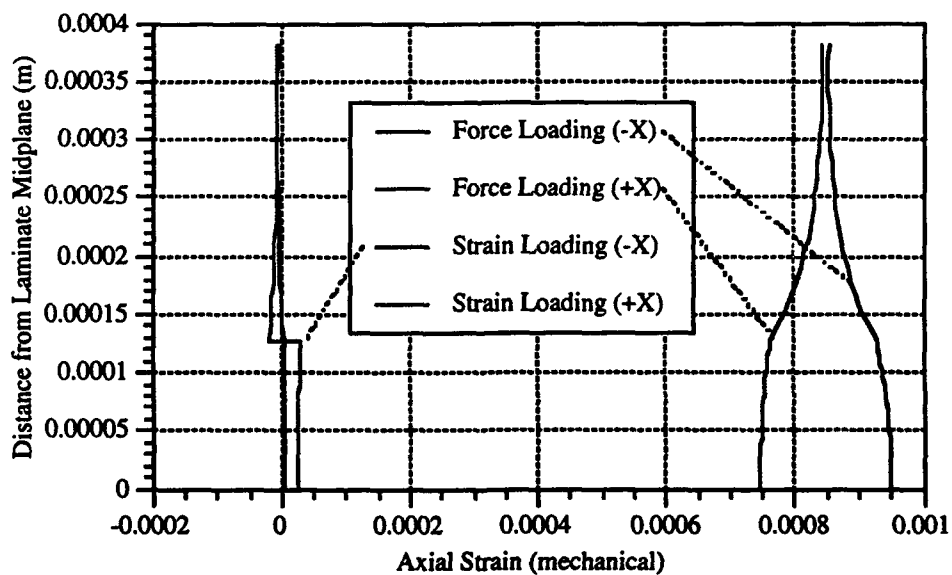


Figure 6: Interface Axial Strains through Laminate Thickness

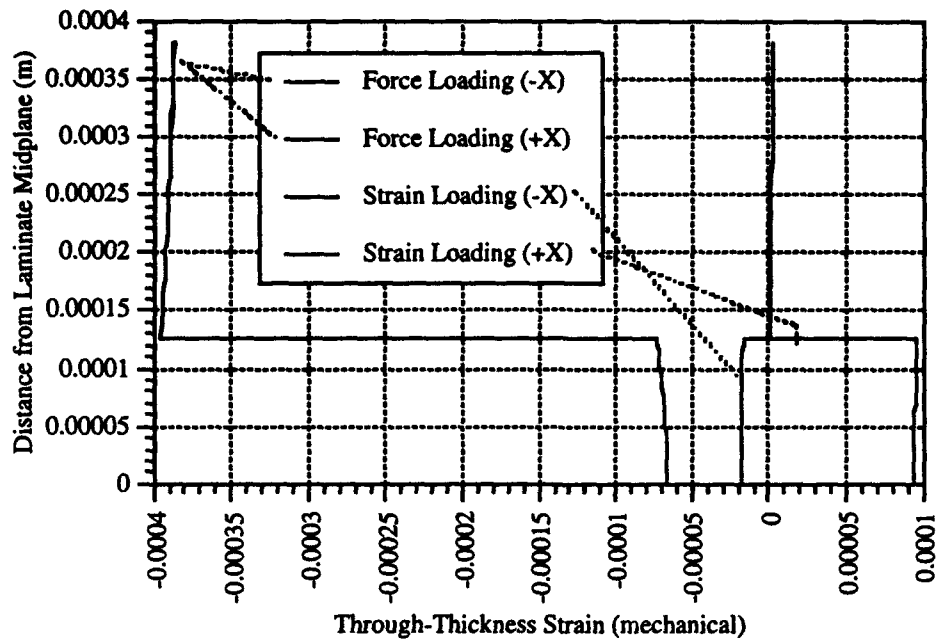


Figure 7: Interface Through-Thickness Strains through Laminate Thickness

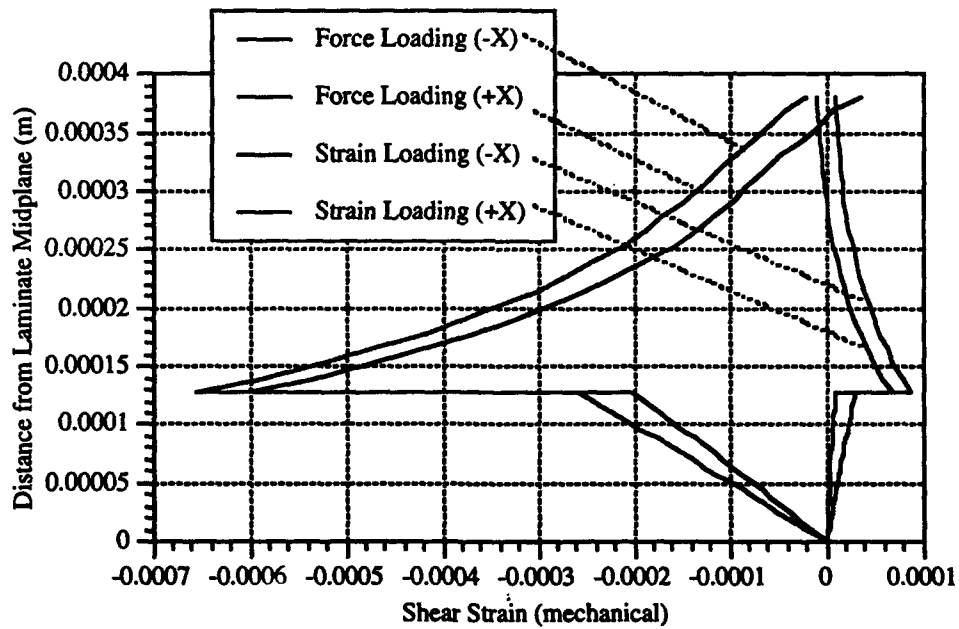


Figure 8: Interface Shear Strains through Laminate Thickness

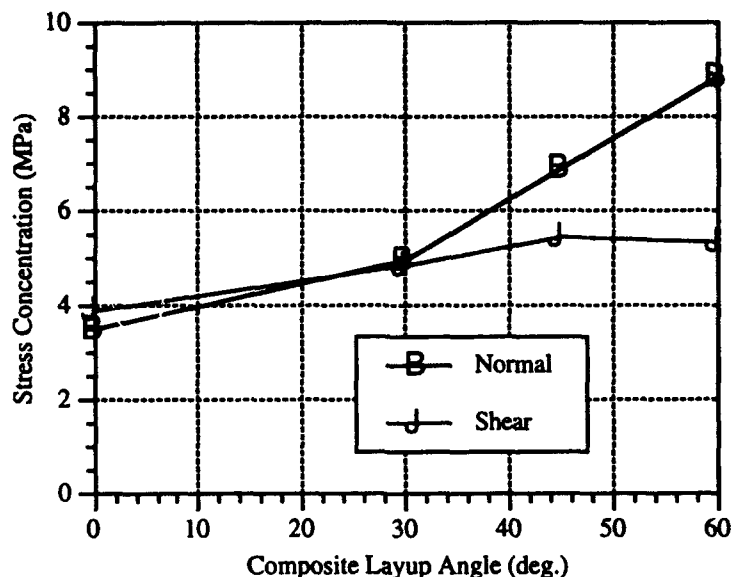


Figure 9: Strain Concentration vs. Lamination Angle – Applied Stress Loading

### 3.1.3 Influence of Host-Material Orientation

Subsequent analyses employing the analytical model were run to assess the effects of composite lamination angle on the severity of stress gradients in the intelligent material system. The purpose of these analyses was to recommend design configurations that might minimize interfacial stress concentrations.

Figures 9 and 10 show maximum through-thickness (normal) and shear interfacial stress concentrations versus lamination angle of the host composite material (note that the composite laminate is *balanced* with  $[\pm\theta]$  plies to accommodate the two-dimensional assumptions of the analytical model). These figures show that both normal and shear stress concentrations grow under applied axial loadings as the laminate axial stiffness drops. However, normal stress concentrations are relatively insensitive to lamination angle under activation of the intelligent material wafer. Shear stress concentrations actually reduce with increasing off-axis laminate angle under induced-strain loading.

The effect of the variations shown in Figures 9 and 10 is to recommend axially dominated laminates for axial loadings. As noted in §3.1.2, interface normal stresses are expected to dominate for initiation of interlaminar cracks under applied, in-plane loadings. Aligning the composite-material layers with this loading provides minimum normal- and shear-stress concentrations. Furthermore, no appreciable reduction in normal-stress concentration can be gained by off-axis lamination even in the case where only induced-strain loadings are present, as seen in Figure 10. However, if the material loading is to be dominated by strain activation of the intelligent material, reductions in shear-stress concentrations could be achieved by increasing the composite

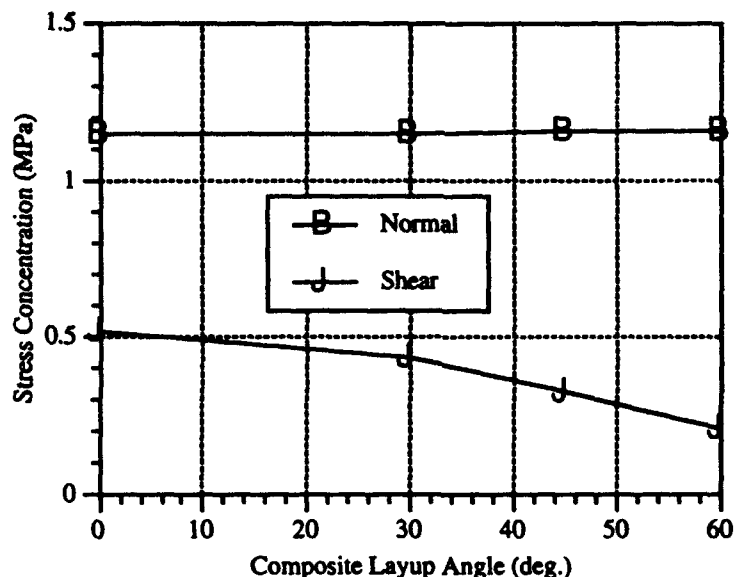


Figure 10: Strain Concentration vs. Lamination Angle - Induced Strain Loading

lamination angle.

Another instructive way to view these results is with respect to the relative stiffness of the composite host material in axial and through-thickness shear directions. As the lamination angle is increased, the transverse shear stiffness  $C_{55}$  increases relative to the axial stiffness  $C_{11}$ . Figures 11 and 12 show the effect of this stiffness ratio. These figures indicate that use of stiffer composite matrix materials raise normal- and shear-stress concentrations under applied external loadings, and lower the shear-stress concentration under pure induced-strain loading. Accordingly, if significant external loadings are to be applied to the intelligent material system, interfacial stresses are reduced as compliance of the host-composite matrix is increased.

#### 3.1.4 Requirements for Model Discretization

The analyses presented in §3.1.2 were also employed to determine suitable discretizations for finite-element models used in crack-growth studies. Two discretization requirements were enforced. First, the finite-element model was required to span a length sufficient to capture the entirety of the strain gradients either side of the material interface. Examination of Figures 3 to 5 shows this length to be  $\pm 3$  to 5 mm from the interface.

Second, the finite-element model was required to have sufficiently small elements to enable capture of the strain-gradient magnitudes at the material interface. For linear-displacement (constant strain) elements, a minimum of two elements are required to capture a linear strain gradient. To match the 8<sup>th</sup>-order gradient predicted by the analytical model, a minimum of nine, constant-strain elements would be re-



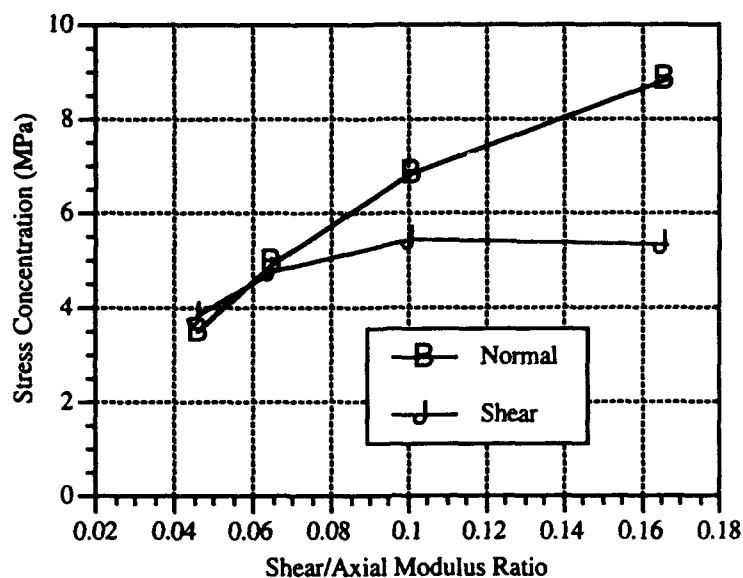


Figure 11: Strain Concentration vs. Stiffness Ratio - Applied Stress Loading

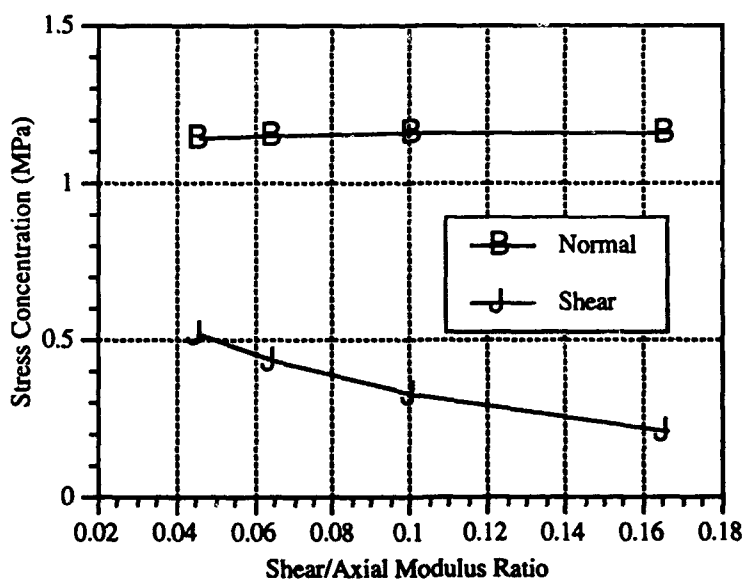


Figure 12: Strain Concentration vs. Stiffness Ratio - Induced Strain Loading

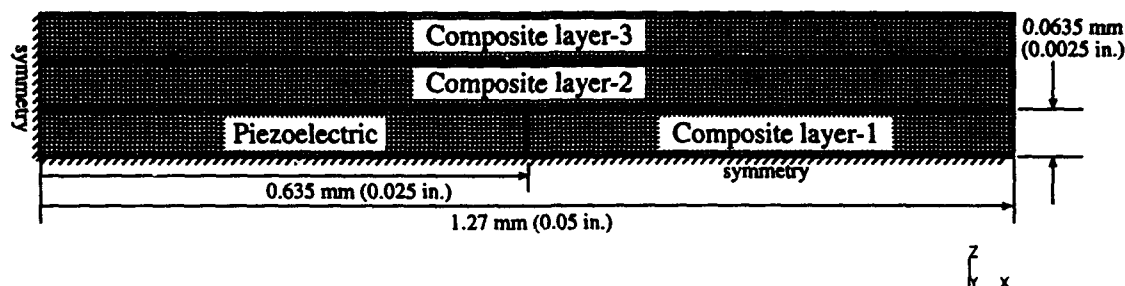


Figure 13: Intralayer embedded FEM model

quired. Capturing the strain gradient predicted by the analytical model thus requires a minimum of nine elements over the first millimeter on either side of the interface. Maximum element dimension according to this criterion is roughly 0.1 mm, or about 40% of a layer thickness.

Through-thickness gradients must also be captured in the finite-element model. To capture the third-order strain field of the analytical model requires a minimum of four constant-strain elements through the thickness of each layer. This translates into a maximum element dimension of roughly 0.032 mm (0.00125 in), or about one-third of the minimum required axial dimension.

An element dimension of  $0.25 \cdot 10^{-3}$  inch (0.006 mm) was chosen for the finite-element models used in this study. This dimension exceeded the discretization requirement established by the analytical model by over a factor of two, as the layer thickness employed in the finite-element model was half that modeled analytically.

## 3.2 Finite Element Models

### 3.2.1 Intralayer Embedment

#### DESCRIPTION

The finite element model used the configuration shown in Figure 13. This model, like the analytical model, represents a piezoelectric wafer embedded within a graphite-epoxy laminate. For comparison purposes, the material properties used were the same orthotropic properties as those used for the analytical model. All layers of the graphite-epoxy composite had a fiber lamination angle of zero. To reduce computation, the length of the specimen was smaller than the analytical model.

The entire model was constructed of plate elements  $6.35 \mu\text{m}$  ( $0.25 \cdot 10^{-3}$  in.) on a side and 1 mm (0.0394 in.) thick. Model symmetry was used so only the upper right quadrant of the system was actually modeled. Coincident nodes were used along the vertical interface between the piezoelectric and the adjacent horizontal layer of composite. These nodes were left unattached for all runs of the model because no bonding would be expected along this interface. Coincident nodes were also used along the horizontal interface between the top of the piezoelectric and the adjacent composite, and between adjacent layers of the composite at the same height as the piezoelectric. All horizontal coincident nodes were attached for the initial runs. The nodes between adjacent composite layers were then released in subsequent runs to examine crack growth.

An axial stress of 1.75 MPa (254 psi) was applied to right-hand edge of the model. Thermal loadings were used to simulate induced piezoelectric strains. A  $\Delta T$  value of 100 was used for all cases, along with horizontal and vertical thermal expansion coefficients of  $-9.606\text{E-}7$  and  $2.2441\text{E-}6$  ( $\text{K}$ ) $^{-1}$ , respectively. This allowed a direct correspondence between temperature and applied voltage. The opposing signs of the coefficients provided for piezoelectric expansion along one axis while it contracted along the other. The applied piezoelectric strain for all cases was  $\epsilon_1^p = -9.6 \cdot 10^{-6}$  and  $\epsilon_3^p = 22.4 \cdot 10^{-6}$ .

The final model size was determined by building a long model and examining the locations of essentially zero shear strain given the combination of the applied loads above. Figure 14 is a gray-scale image of the final model showing that the shear strains effectively go to zero within three thicknesses of the piezoelectric wafer. Also, the analytical model predicted that a length to thickness ratio of 7.9 for the piezoelectric wafer would be necessary for complete stress analysis. The final FE model has a length to thickness ratio of 10.

## RESULTS - STRESS GRADIENTS/DEFORMATIONS

Once final model size was determined, eleven runs were performed in which coincident nodes along the composite layer interface were released one by one. An initial run was made with no horizontal nodes released. The results of this run supplied displacements and node restraint forces for the run in which the first coincident nodes were released. Figures 15 and 16 show the nodal displacements given by these first two runs. Work terms were calculated from the new displacements of the second run. This was repeated nine more times. Figure 17 shows the displacement field after four nodes were released. As expected, the percent change from one release to the next for the mode I (normal-tension) displacements have drastically diminished while the percent change of the mode II (shear) displacements have not been much altered.

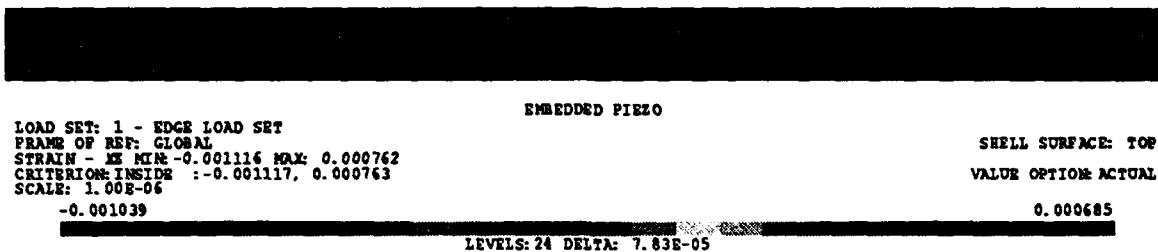


Figure 14: Shear strains in the initial FEM model

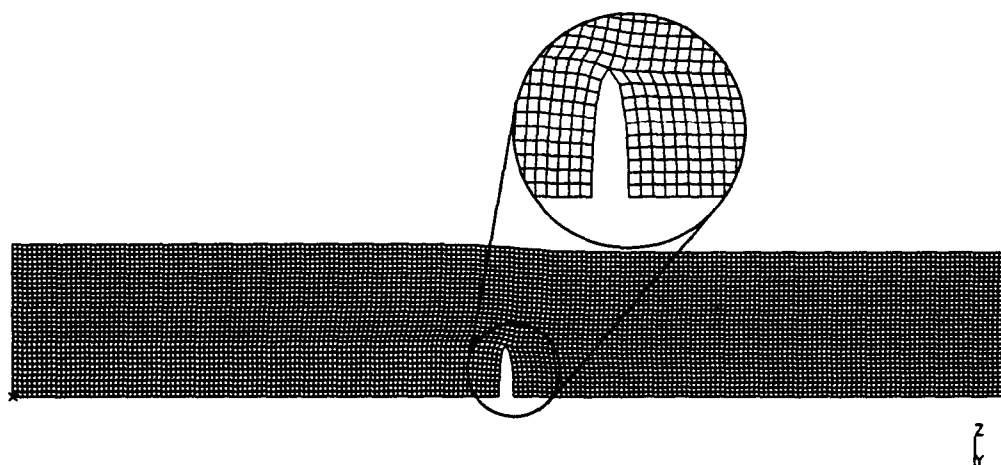


Figure 15: Nodal displacements with no horizontal nodes released

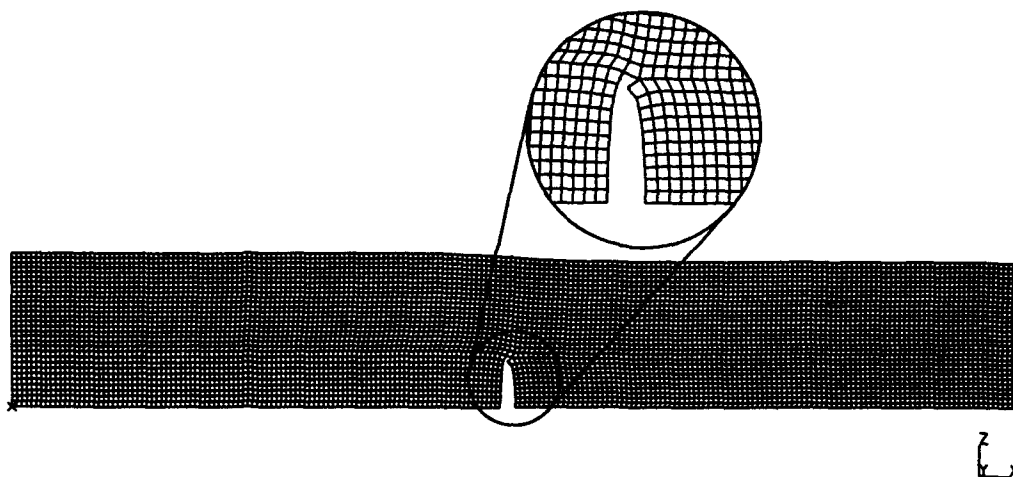


Figure 16: Nodal displacements with one horizontal nodes released

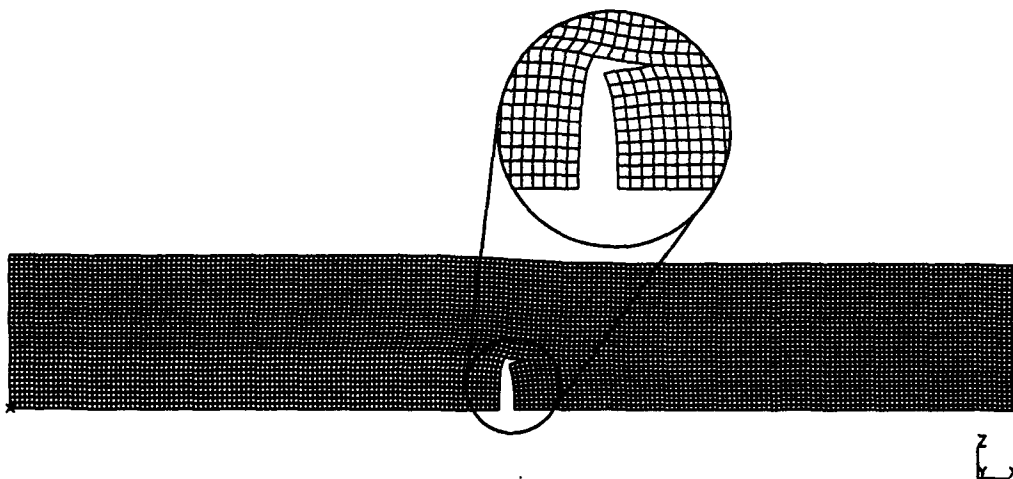


Figure 17: Nodal displacements with four horizontal nodes released

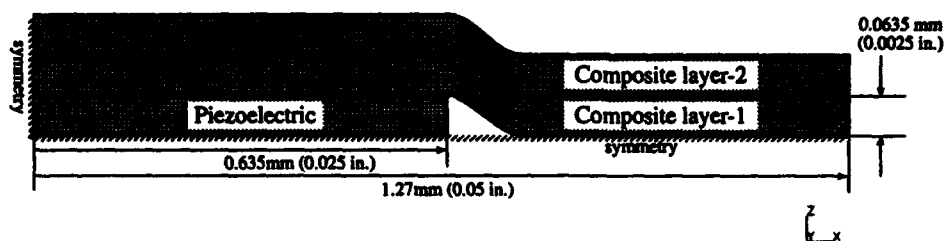


Figure 18: Interlayer embedded FEM model

### 3.2.2 Interlayer Embedment

#### DESCRIPTION

The model used in the previous intralayer embedment was modified to represent a piezoelectric wafer embedded between two layers of graphite-epoxy laminate. Figure 18 shows the modified model. Coincident nodes were placed along the horizontal interface along the top of the piezoelectric and the adjacent composite. These nodes were attached for initial runs and then released in subsequent runs to examine crack growth between the piezoelectric and composite. The nodes along the horizontal plane of symmetry between composite layers were also held and then released to study crack growth between composite layers.

The previous intralayer configuration used an axial loading of 1.75 MPa. This was done to try to equilibrate the effects of both the axial load and the induced piezoelectric strain. After examination of the results, it was determined that the axial load was the prime contributor to crack growth after the first node was released. It was therefore decided to increase the magnitude of the axial load for the interlayer configuration 100-fold to 175 MPa (25.4 ksi). This was applied in separate runs for both tension and compression. The induced piezoelectric strains were not changed in magnitude from those used in the intralayer configuration, although the sign of  $\Delta T$  was reversed for all runs under axial compression. This configuration - axial compression loading combined with negative piezoelectric strain in the Z direction - gave the highest nodal restraint forces.

#### RESULTS - STRESS GRADIENTS/DEFORMATIONS

A total of fifteen runs were performed:

- three runs with zero axial load
- five runs with tensile axial load in which single point constraints for the nodes along the line of horizontal symmetry were released one by one
- five runs with compressive axial forces in which the coincident nodes along the piezoelectric-composite layer interface were released one by one

As with the intralayer configuration, an initial run was made for both the tensile and axial compression load cases with no nodes released. Then, each successive run, tensile as well as compressive load cases, built on the run before it to determine work terms (release force · relative displacement) in both the X and Z directions for each node released. Figures 20 and 21 show the model in tensile and compressive loadings, respectively.

The interesting note from the tensile case is that the node release force for the first node between the composite layers was positive in the Z direction. This indicates that at this point, where crack initiation might be expected, there is actually a compressive force that inhibits mode I cracking. However, subsequent nodes to the right of this experience a tension force tending to cause cracking.

Note also that the piezoelectric in Figure 20 has been displaced in the positive X direction even though the induced strain for this case was in the positive Z, negative X direction. This positive displacement can be attributed entirely to the large applied axial tensile stress that overwhelms the induced piezoelectric strain. Similarly, the piezoelectric in Figure 21 has been displaced in the negative X direction even though the induced strain for this case was in the positive X direction.

The axial compression load condition was the more interesting as the node release forces for mode II crack growth were an order of magnitude higher than the next closest release rates of any configuration. Figure 22 shows the displacement field under compressive axial load after four nodes were released between the piezoelectric and composite interface.

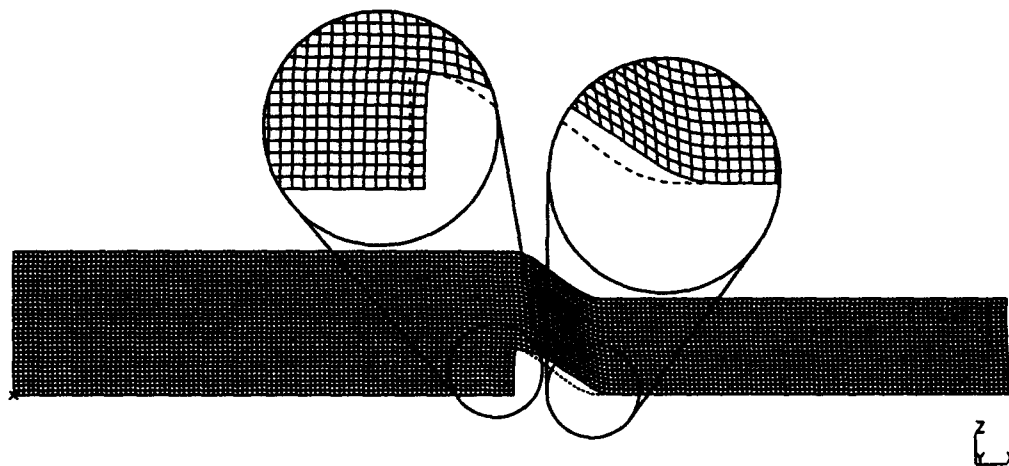


Figure 19: Nodal displacements with no nodes released; axial load in tension

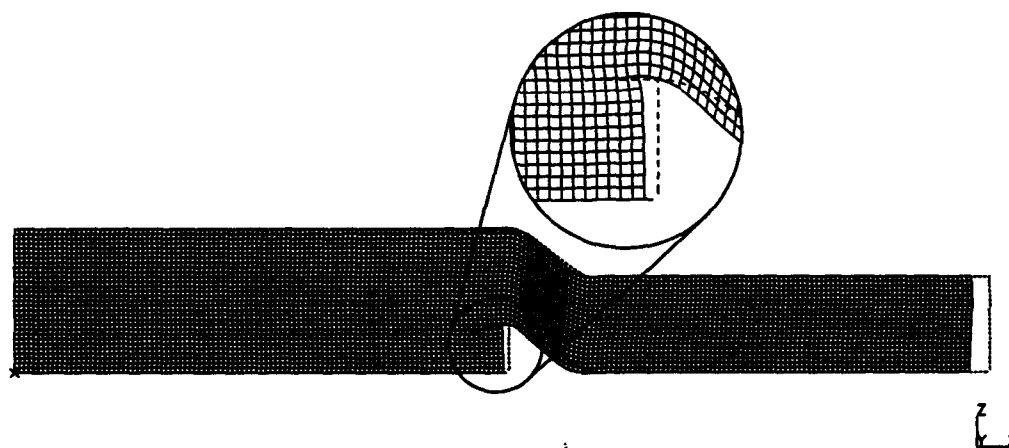


Figure 20: Nodal displacements with no nodes released; axial load in compression



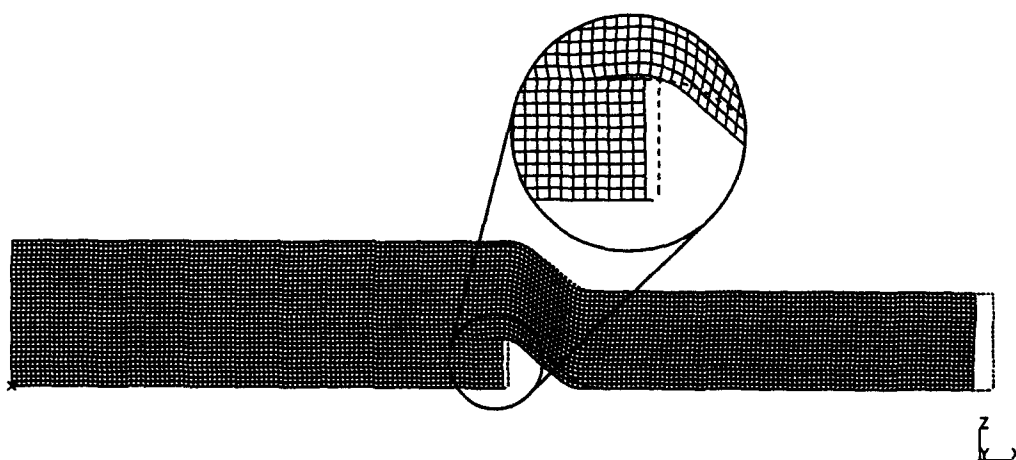


Figure 21: Nodal displacements with four nodes released; axial load in compression

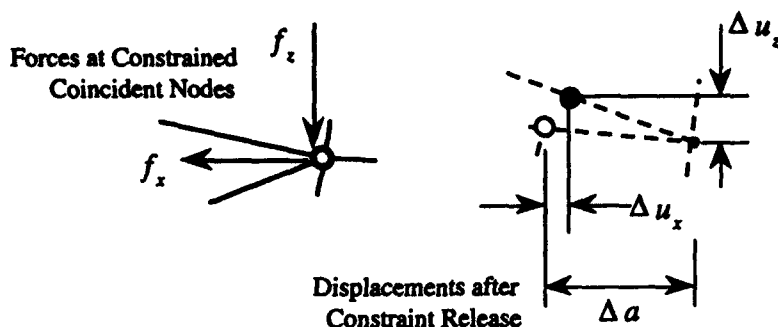


Figure 22: Quantities for Calculating Strain Energy Release Rates

## 4. Task 3 – Interface Failure Models

The finite-element models described in §3.2 were used to assess crack propagation behavior in the intelligent material system. The method employed for this assessment computed strain-energy release rates for growing cracks by calculating the work done by crack-closure forces associated with nodal displacement constraints along a predefined crack path. Energy release rates were investigated for two cases; one in which the intelligent material element (piezoelectric wafer) was inserted into a layer of the host composite material ("intralayer" embedment), and one in which the intelligent material element was inserted between layers of host material ("interlayer" embedment). In the former case, energy release rates were calculated for a combined piezoelectric actuation and applied axial tension loads. In the latter case, both tensile and compressive axial loads were applied in conjunction with the piezoelectric actuation to assess crack propagation at two sites in the material system.

### 4.1 Calculation of Strain-Energy Release Rates

Strain-energy release rates were computed from the finite-element model data using a node-release method. This method computed the work released by releasing a nodal displacement constraint along the crack path, as illustrated in Figure 22. The method involves comparing results of two analysis steps. First, constraint forces are recorded when the crack is held closed by a constraint applied to enforce displacements at coincident nodes along the crack path to be equal. Second, the constraint is released and the resulting relative nodal displacements are recorded. The work released by growing the crack to the next coincident-node pair along the crack path is then computed as

$$\Delta W = \frac{1}{2} (f_x \Delta u_x + f_z \Delta u_z). \quad (16)$$

The node-release method allows the relative contribution of mode I (normal tension) and mode II (shear) stress intensities to be assessed. The first work term on the right-hand-side of eq. (16) represents the shear (mode II) contribution, while the second represents the tensile (mode I) contribution. The strain-energy release rates are thus

$$\begin{aligned} G_I &= \frac{1}{2} f_z \Delta u_z \\ G_{II} &= \frac{1}{2} f_x \Delta u_x \end{aligned} \quad (17)$$

For very long cracks, an expression derived by Wisnom<sup>1</sup> can be employed to assess the asymptotic, mode II strain-energy release rate:

$$G_{II_s} = \frac{\sigma_1^2 h t}{4 E_{11} (h - t)} \quad (18)$$

where  $\sigma_1$  is the applied axial stress,  $h$  is the total thickness of the laminate,  $t$  is the thickness of the material region between the growing cracks on either side of the midplane of the laminate, and  $E_{11}$  is the composite axial modulus. For the present models, which represent one half of Wisnom's model through the thickness, the asymptotic strain-energy release rate is one-half that given in eq. (18), and takes a value of

$$\begin{aligned} G_{II_s} &= 1.875 \cdot 10^{-3} \frac{\sigma_1^2}{E_{11}} \text{ in} \\ &= 4.763 \cdot 10^{-5} \frac{\sigma_1^2}{E_{11}} \text{ m} \end{aligned} \quad (19)$$

for the properties and dimensions employed here. It is useful to examine the value of  $G_{II}$  relative to its asymptotic value to determine how far a delaminating crack must grow before the delamination propagates catastrophically.

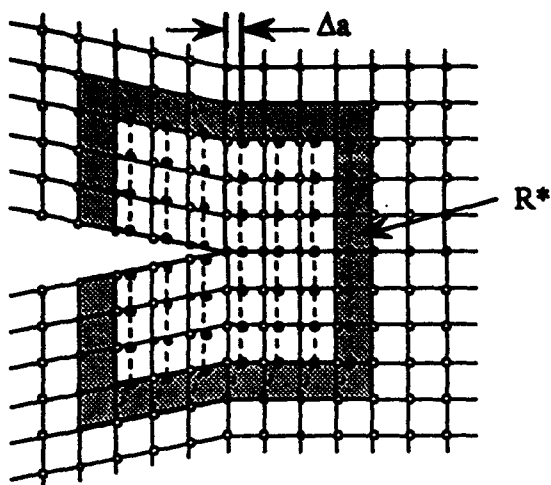
## 4.2 Virtual Crack Extension

### 4.2.1 Theory

The virtual crack extension method<sup>2</sup> may be used to compute strain energy release rates along highly stressed interfaces in material systems such as those studied here.

<sup>1</sup>Wisnom, M. R., "Delamination in Tapered Unidirectional Glass Fibre-Epoxy under Static Tension Loading," AIAA-91-1142-CP, *Proc. 32nd Structures, Structural Dynamics and Materials Conference*, April 1991, p. 1162

<sup>2</sup>Hellen, T. K., "On the Method of Virtual Crack Extensions," *Int. J. Num. Method. Eng.*, Vol. 9 (1975) p. 187.



Virtual Crack Extension  $\Delta a$

$$G = \frac{1}{2\Delta a} [U(d + \Delta a) - U(d - \Delta a)] - \frac{1}{2\Delta a} [V(d + \Delta a) - V(d - \Delta a)]$$

Figure 23: Virtual Crack Extension Computation of Strain Energy Release Rate

Evaluation of these release rates can lead to predictions of the likelihood of compromising material and structural integrity by propagating interfacial cracks and delaminations into the host material.

The method relies on a relatively good description of the stress state in a region somewhat removed from a hypothesized crack tip to compute an approximation to the instantaneous strain energy release rate  $G$ . If this rate exceeds the material limit, the crack is grown to the next mesh point and the analysis is continued. Some recent research has shown very good agreement between analytical VCE models and experiments for delamination in certain composite constructions.<sup>3</sup>

Practically speaking, virtual crack extension must be implemented in the context of a finite element model with good detail around the crack tip, as illustrated in Figure 23. A stress analysis is performed, resulting in a set of nodal displacements  $d$ . A ring of elements is selected that surrounds the crack tip but is several elements away from it. An energy release rate  $G$  is computed by applying a small rigid-body displacement to the nodes on the inside of the ring, shown as a horizontal motion in the figure for mode I crack growth. Thus if  $r$  is a vector of unit motions in the specified direction along the inner ring of nodes, we have

$$G = \frac{1}{2\Delta a} [U(d + \Delta a r) - U(d - \Delta a r)] - [V(d + \Delta a r) - V(d - \Delta a r)] \quad (20)$$

where  $U$  represents the strain energy developed as a result of this fictitious movement

<sup>3</sup>Wisnom, op. cit.

and  $V$  represents work done by external loads.

### 4.2.2 Development

Assuming no loads applied to the ring of elements and hence no work term  $V$ , the required strain energy values can be obtained using the stiffness matrix for the ring of elements:

$$\begin{aligned} U(\mathbf{d} + \Delta \mathbf{a} \mathbf{r}) &= \frac{1}{2}(\mathbf{d} + \Delta \mathbf{a} \mathbf{r})^T \mathbf{K}(\mathbf{d} + \Delta \mathbf{a} \mathbf{r}) \\ U(\mathbf{d} - \Delta \mathbf{a} \mathbf{r}) &= \frac{1}{2}(\mathbf{d} - \Delta \mathbf{a} \mathbf{r})^T \mathbf{K}(\mathbf{d} - \Delta \mathbf{a} \mathbf{r}) \end{aligned} \quad (21)$$

Expanding,

$$\begin{aligned} U(\mathbf{d} + \Delta \mathbf{a}) &= \frac{1}{2} \mathbf{d}^T \mathbf{K} \mathbf{d} + \Delta \mathbf{a} \mathbf{d}^T \mathbf{K} \mathbf{r} + \frac{1}{2} (\Delta \mathbf{a})^2 \mathbf{r}^T \mathbf{K} \mathbf{r} \\ U(\mathbf{d} - \Delta \mathbf{a}) &= \frac{1}{2} \mathbf{d}^T \mathbf{K} \mathbf{d} - \Delta \mathbf{a} \mathbf{d}^T \mathbf{K} \mathbf{r} + \frac{1}{2} (\Delta \mathbf{a})^2 \mathbf{r}^T \mathbf{K} \mathbf{r} \end{aligned} \quad (22)$$

so that

$$G = \frac{2\Delta \mathbf{a} \mathbf{d}^T \mathbf{K} \mathbf{r}}{2\Delta \mathbf{a}} = \mathbf{d}^T \mathbf{K} \mathbf{r} \quad (23)$$

a result which is seen to be independent of the displacement increment  $\Delta \mathbf{a}$ .

Note that the vector of nodal point forces generated by the elements in the ring is  $\mathbf{f} = \mathbf{K} \mathbf{d}$ , so that the expression reduces to

$$G = \mathbf{f}^T \mathbf{r} \quad (24)$$

Recognizing that  $\mathbf{r}$  is a vector of unit values corresponding to translations of each of the two rings of nodes in a specified direction (horizontal in Figure 23), we see that  $G$  is simply the sum of the forces applied by the elements in the ring to the nodes on the inner ring. The forces from one side of the ring tend to cancel those on the other side, and this suggests that considerable precision may be required in performing this calculation.

The foregoing derivation assumed that no loads were applied to any elements in the ring. However, as explained elsewhere, piezoelectric actuation was simulated in the finite element models used in this project by thermally induced strains. Thus there were in fact loads applied to those elements in the ring that represent piezoelectric material. In order to account for this one must replace  $\mathbf{f}$  by  $\mathbf{f} + \mathbf{g}$  where  $\mathbf{g}$  is a vector of nodal loads due to the fictitious temperature rise. These load vectors are generated by finite element codes by integration of the thermal stresses of the form  $E\alpha\Delta T$  over the area of the element. The energy release rate is then

$$G = (\mathbf{f} + \mathbf{g})^T \mathbf{r} \quad (25)$$

Note that this term must be divided by the thickness of the elements used to represent the "slice" of composite material in order to obtain an energy release rate per unit of newly opened crack area. It is this figure which is to be compared with critical values for a particular material.

#### 4.2.3 Programming

The foregoing calculations were programmed for use with UAI/NASTRAN for analysis and I-DEAS for generation and display. A Fortran program was written to perform the following functions:

1. Accept user definitions of the inner and outer node rings as "groups" generated in I-DEAS.
2. Obtain displacements for these nodes from a "punch" file written by the main NASTRAN stress analysis.
3. Open a new NASTRAN bulk data file to be used by the DMAP program described below in calculating energy release rates.
4. Write displacements to this file in DMIG format.
5. Write GRID entries for all the ring nodes, CQUAD4 entries for the wing elements, and associated property and material entries.
6. Write executive control and case control data to generate thermal loads and to access the required DMAP program.
7. Execute the NASTRAN run.
8. Find and display the strain energy release rate in the print file.

The DMAP program consisted of about 30 lines that perform the following operations:

1. Read node and element data and generate the stiffness matrix  $K$  for the ring elements only.
2. Generate thermal loads.
3. Read displacements  $d$  from DMIG bulk data entries.
4. Compute elastic forces by the matrix multiplication  $f = Kd$ .
5. Compute a thermal load vector  $g$  from temperature data, thermal expansion coefficients, and element geometry.

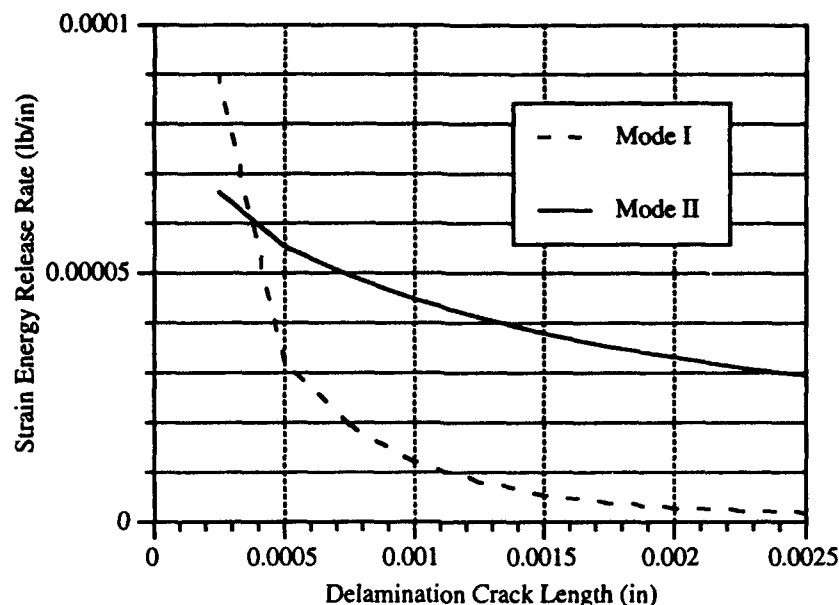


Figure 24: Intralayer Embedded Strain Energy Release Rates

6. Compute and print  $G = (f + g)^T r$ .

There was not sufficient time in Phase I to demonstrate virtual crack extension on test cases. This will be pursued in Phase II.

## 4.3 Results

### 4.3.1 Intralayer Embedded Element

Strain-energy release rates predicted by the intralayer-embedment model are shown in Figure 24. The mode I energy release rate is considerably higher at crack initiation than the mode II release rate. However, as the crack grows beyond a small length, mode II release rates dominate.

Note that the energy release rates shown in Figure 24 are significantly lower than critical strain energy release rates for conventional polymer composites. Typical composite interlaminar strain energy release rates fall in the range 250-450 N/m (~1.5-3.0 lb/in). The peak rates calculated by the present analyses fall some 20,000 times below that range. However, the intralayer-embedded finite-element model considered applied tensile stresses of only 254 psi, a very low level relative to the composite's capability. Wisnom's analysis shows that one should expect mode II energy release rates to be proportional to the square of the applied tensile stress. Thus, critical energy release rates might be achieved in the modeled laminate for tensile loadings of the order of 38-45 ksi, corresponding to roughly half the strength of the unidirectional composite material.

Mode I energy release rates are determined chiefly by interlaminar tension rather than shear. Review of Table 2 reveals that stress contributions of piezoelectric and applied tensile loadings are approximately equal at a level of 5000 psi applied axial stress. Thus, most of the mode I energy release at crack initiation is due to the action of the piezoelectric element for the relatively low applied stress of 254 psi. However, the mode I energy release rate will be made critical only by increasing the applied loading, since the induced strain loading applied in the model is very close to the maximum available from the piezoelectric material. Assuming that mode I energy release rate scales with the square of interlaminar tensile stress, an elementary analysis shows that critical energy release rates might be achieved for applied loadings between 11-15 ksi (76-104 MPa). Such loadings would result in initiation of a delaminating crack, but would contribute little to its growth beyond a short length because of the rapid decay of mode I energy release rate, as shown in Figure 24.

As mentioned above, an asymptotic value for mode II energy release rate can be computed based on the applied stress. Figure 25 shows the ratio of the mode II energy release rate to its asymptotic value for the intralayer-embedded element case. The solid line in this figure represents the data also presented in Figure 24. The dashed line is a semi-log extrapolation of the trend, indicating an estimate of the crack length at which the asymptotic value will be achieved. Once the crack grows to the critical length, applied stresses sufficient to exceed  $G_{IIc}$  would cause the delamination to propagate catastrophically. This length is projected to be, at minimum, roughly 0.01 in for the intralayer-embedded configuration analyzed. As this is a small value relative to the sensitivity of inspection methods, applied loadings should be kept below

$$\sigma_1 < \sqrt{4G_{IIc}E_{11} \frac{(h-t)}{ht}} \quad (26)$$

for reliability. Here,  $h$  is the total thickness of the laminate, and  $t$  is the aggregate thickness of all intelligent-material elements embedded through the thickness at the critical location. For the case analyzed presently, the stress limit falls in the range 120-170 ksi, or roughly a factor of three above the stress level at which delamination is predicted to begin to be governed by mode II behavior.

#### 4.3.2 Interlayer Embedded Element

In the case of interlayer embedment, two locations in the intelligent, composite material system are potentially critical. These locations are shown in Figure 26, and lie along the interface between intelligent and host composite materials, and at the point where the host composite material is joined beyond the extent of the embedded element. Strain-energy release rates at both of these locations were investigated. The model considered applied axial loadings of  $\pm 25$  ksi.

Mode I and mode II strain-energy release rates predicted for delamination of the



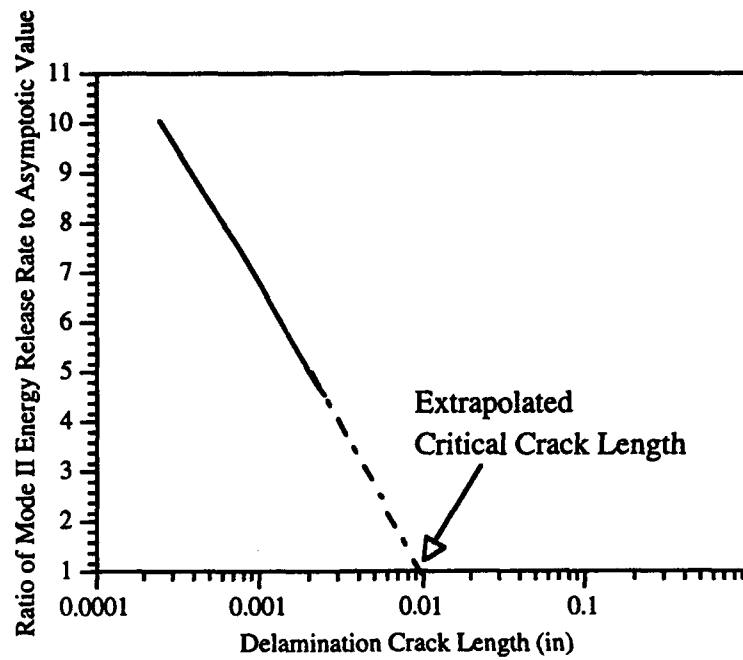


Figure 25: Intralayer-Embedded Mode II Strain Energy Release Rate Ratio

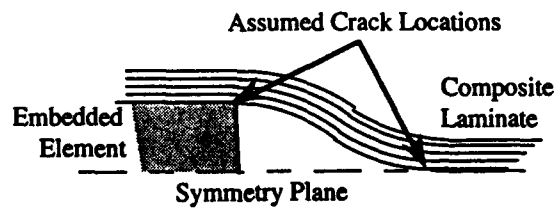


Figure 26: Interlayer-Embedded Assumed Crack Locations

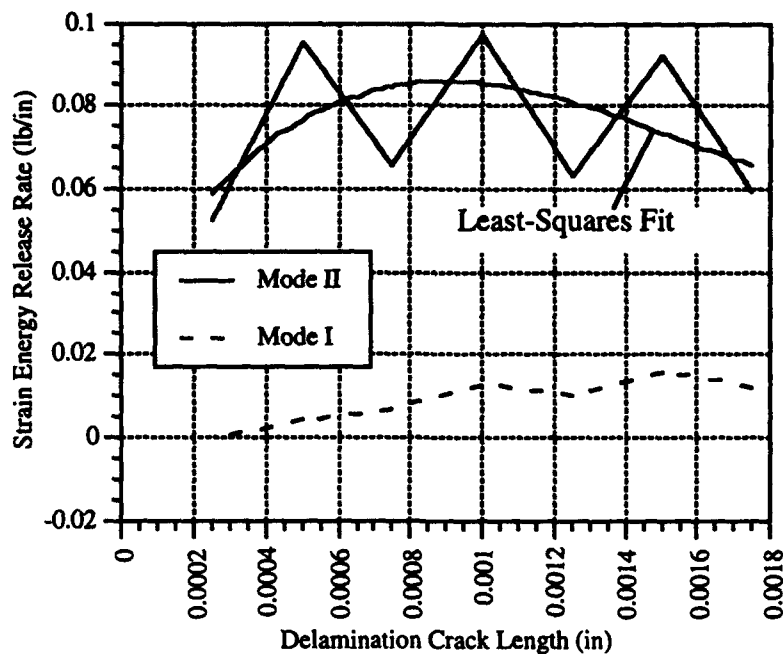


Figure 27: Strain Energy Release Rates along Piezoelectric Wafer Interface

embedded element from the host composite (loaded in compression) are shown in Figure 27. This figure shows that much higher values are obtained in mode II than mode I, although the model predicted these values somewhat erratically. Further investigation revealed that the oscillatory predictions were due to oscillations in the calculated values of relative crack-sliding displacements. A least-squares fit of the predictions is also illustrated in this figure. This shows an onset of unstable, mode II crack growth up to a length of roughly 0.001 in, followed by stable growth,

Figure 28 shows strain-energy release rates calculated at the point where composite layers are brought together outside the embedded-material region. In the present model, this location lies on a plane of enforced symmetry, so crack growth is possible only mode I.

An interesting result was found for the configuration analyzed. Crack initiation must occur under axial compressive loadings, as this loading produces interlaminar tension at the crack tip. However, after growing a small distance, the stress field at the crack tip reverses, and the crack grows only under tensile applied loads. Although figure 28 shows this subsequent crack growth to be unstable, the linear model did not consider the effects of crack-closing displacements. As axial tension is applied to the configuration, the crack closes at the original point of initiation, lowering tensile stresses at the crack tip. This effect must be investigated using a nonlinear model to characterize strain-energy release rates under applied tensile loadings.

Examination of figures 27 and 28 do show that strain-energy release rates for delamination of the embedded, intelligent material element from the host composite

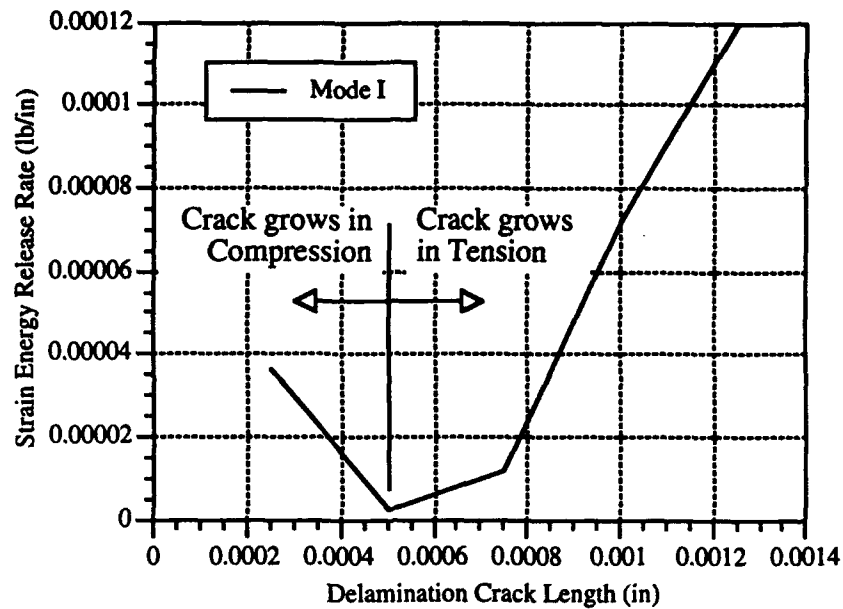


Figure 28: Strain Energy Release Rates along Composite Interface

material are much higher than for delamination within the host material itself. This delamination is dominated by mode II behavior, and would be expected to reach  $G_{IIc}$  at an applied stress level of roughly 100 ksi.

## **5. Task 4 - Candidate Experimental Configurations**

### **5.1 Requirements**

The integrity of intelligent material systems in service will ultimately be ensured by a base of analytical and practical experience validated by extensive testing. The objectives of any testing program must include not only validation of theories and models, but also discovery of unknown factors influencing material performance. While this program has investigated some of the salient aspects of intelligent materials integrity, a subsequent program of experimentation should be undertaken to assess the validity of the present results (and similar approaches pursued by others), and to determine the engineering soundness of the assumptions made in such models. Accordingly, this section examines some basic requirements and approaches for experimental investigations of the integrity of intelligent materials and structures.

First and foremost, experimental articles should be built to replicate configurations likely to be employed in practice. These may include intralayer, interlayer or fiber-embedded elements, surface-attached elements, or even elements incorporated directly into the host composite material (e.g., whiskers). Conventional structural composite materials should be employed as host materials.

Second, experimental articles should be subjected to the environments and conditions they are likely to see in service. These include thermal, atmospheric and loading environments (both static and dynamic).

Third, sensing schemes must be developed to track the occurrence and progression of damage within the intelligent material system as it is under test. Tracking growth of internal damage will enable detailed validation of analytical models, and will bring to light any important factors that such models may not treat well.

Finally, and perhaps in the longest term, the experimental program should build a database of failure modes and strengths to establish reliable engineering properties for intelligent materials and structures.

### **5.2 Sensing Approaches**

A key issue in any characterization program is the fidelity of sensing elements employed in the experiment. The idea of photoelastic or other interferometric sensing of surface strains or surface "bulging" suggests itself. However, the studies performed so far predict very small surface bulging or changes in surface strains, so that this approach might not detect a crack until it had gotten rather far along.

Another significant finding, as discussed above, was that applied loading has a greater influence than piezoelectric actuation. This suggests that procedures "conven-

tionally" used for detection of delamination would also be applicable to delaminations associated with embedded elements.

Through-the-thickness acoustical measurements should also be considered. The rather small layer thicknesses suggest possible problems with spatial resolution in this approach (i.e., acoustic wavelengths).

In Phase II, the studies initiated in Phase I will be continued, partially for the purpose of designing a suitable experiment. Three-dimensional models may be used in order to predict two-dimensional surface responses. Also, we will research current sensing methodologies, both interferometric and acoustical.

### 5.3 Discussion

Perhaps the most important physical quantity to be assessed by experiments in this area is the value of the critical strain-energy release rate between the dissimilar intelligent and host composite materials. This quantity will allow assessment of loadings and crack dimensions that may cause catastrophic propagation of interface cracks which decouple the intelligent material element from its host material. Also, the possibility exists that the critical mode II energy release rate for a candidate ceramic active material may dominate the interfacial failure. In this case, the ceramic may be found to have lower capability in this mode than the host composite material, causing loads to be limited to well below the capacity of the host composite in order to preserve the active integrity of the intelligent material system.

If energy-release values  $G_{IIC}$  are found to be lower within the host material than across host-intelligent material interfaces, then experimental characterization of flaw propagation due to external loadings need only consider the presence of a stiff element mimicking the intelligent material since its activation plays a relatively minor role in interlaminar crack propagation in the host material.

## 6. Conclusions

### 6.1 Observations

The following observations may be drawn from the results of this study:

1. The presence of stiff, active material elements in laminated composites causes significant concentrations of interlaminar tension and shear stresses and strains at the interfaces between the two materials. The magnitudes of tension and shear concentrations caused by inducing strains in the active element are roughly equivalent. However, the magnitude of the interlaminar shear stress concentration is roughly twice that of the interlaminar tension stress concentration when in-plane, external loadings are applied to the host material.
2. For cases in which significant external loadings are applied, local interfacial stress gradients and concentrations are dominated by the magnitude of the external loading. The amount of strain that can be induced in conventional ceramic actuator materials is low relative to the capability of the conventional composite materials ( $< 0.1\%$  vs.  $\sim 1\%$ ). Hence, strength-dominated composites will be influenced more by the simple presence of dissimilar, intelligent materials than they will be activation of these materials. Note that this situation may differ for intelligent materials capable of higher activation strains (e.g., shape-memory alloys).
3. Interfacial stress gradients between intelligent and host composite materials occur over distances as small as 4-6 wafer-layer thicknesses from the interfaces.
4. For intelligent composites dominated by external loadings (e.g., aircraft, missiles, launch vehicles), interfacial stress concentrations are minimized by aligning the composite material according to conventional, strength-design procedures. For composites dominated by intelligent-material actuation (e.g., satellite structures), interfacial shear stress concentrations are lowered by increasing transverse shear stiffness in the composite.
5. For intelligent material wafers embedded within composite lamina (intralayer embedment), interface-crack initiation is dominated by mode I behavior, but mode I stress intensity falls off rapidly as the crack advances. Propagation of interlaminar failure is governed by mode I behavior, with relatively the same characteristics as propagating delaminations in conventional composites. Comparing mode II strain energy release rates to their asymptotic values allows an estimate of the critical crack length to be made.
6. For intelligent material wafers embedded between layers of the host, composite material (interlayer embedment), both initiation and propagation of cracks along the material interface are governed by mode II behavior. Interlaminar

interfaces near the embedded, active material but occurring between host material layers can be influenced by either mode I or mode II behavior, although the cases analyzed here admitted only mode I crack growth.

7. Both tensile and compressive loadings are important for crack growth in interlayer embedded material systems. Interlaminar cracking in some areas may be initiated in compression, but tend only to propagate in tension.
8. Crack-closing displacements are important in interlayer embedded configurations due to the coupling of in-plane and out-of-plane forces by the geometric configuration.
9. Strain-energy release rates are significantly higher along the interface between intelligent and host-material elements than between host-material layers away from the embedded element. As such, critical strain-energy release rates along the material interface must be characterized if the integrity of this interface is to be assessed.

## 6.2 Evaluation of Approach and Results

The approach taken in the present study has illuminated some key factors influencing the integrity of intelligent materials systems and structures. In particular, that interfacial crack propagation is governed chiefly by interface shearing (mode II) action, and that interfacial stress concentrations are limited to material regions within a few thicknesses of an embedded, active-material element.

The approach taken to arrive at these results combined analytical and finite-element techniques to assess responses of candidate intelligent material configurations. The analytical model proved appropriate for assessing local stress gradients, and admitted rapid analysis of various material configurations. The finite-element models were sufficiently flexible to allow interface constraints to be easily modified for assessment of strain-energy release rates. However, both of these models can be improved to provide more useful results.

Two specific improvements to the analytical model would make it much more useful for this problem. First, the assignment of Lagrangian constraints should be made at the modeling level, rather than at the numerical level as is now the case. This would allow engineers to specify particular connectivity topologies of interest, rather than just the fully connected, rectilinear topology implemented to date. The analytical formulation would then become useful for studies of stress distributions around interfacial cracks. Second, higher-order, nonlinear strain-displacement should be implemented to assess the effects of geometric nonlinearities on local stresses near interfaces. The polynomial nature of the assumed displacement (and strain) functions in the analytical solution lend themselves easily to such augmentation.

The linear finite-element models used in the present study should be modified to include nonlinear effects associated with geometric stiffness (particularly for the interlayer-embedded case) and with gaps resulting from crack opening displacements. Modeling extensive flaw propagation in the interlayer embedded configurations under cyclic loading requires gap constraints to be considered since extension of cracks near the transition region are associated with opening and closing displacements. Accurate calculation of strain-energy release rates in these cases requires a kinematically correct model of deformations between internal, free surfaces.

Finally, if the present techniques are to provide guidelines for engineering design of intelligent structures, experimental data is needed to assess mode II strain-energy release rates along interfaces between conventional, structural composite materials and practical intelligent materials (e.g., piezoceramics, shape-memory alloys). Without these data, analytical predictions will lack the accuracy needed for their successful application.